University of Alberta

Library Release Form

Name of Author: Sang Hee Han

Title of Thesis: Study of Backgrounds to Black Hole events in the ATLAS Detector

Degree: Master of Science

Year this Degree Granted: 2008

Sang Hee Han
4508 Brisebois Dr. N.W.
Calgary, AB
Canada T2L 2G4

Date: _____

“What you do determines who you are.”

University of Alberta

Study of Backgrounds to Black Hole events in the ATLAS Detector

by

Sang Hee Han

A thesis submitted to the Faculty of Graduate Studies and Research in partial fulfillment of the requirements for the degree of **Master of Science**.

Department of Physics

Edmonton, Alberta
Spring 2008

University of Alberta

Faculty of Graduate Studies and Research

The undersigned certify that they have read, and recommend to the Faculty of Graduate Studies and Research for acceptance, a thesis entitled **Study of Backgrounds to Black Hole events in the ATLAS Detector** submitted by Sang Hee Han in partial fulfillment of the requirements for the degree of **Master of Science**.

Dr. Douglas M. Gingrich (Supervisor)

Dr. Vincent Gaudet (External)

Dr. Douglas R. Schmitt

Dr. James L. Pinfold

Date: _____

To my husband, Wei-yuan, Daniel Ting

Abstract

It is planned that the Large Hadron Collider (LHC) will start running in 2008. Protons from opposite directions will collide at the interaction point with a centre-of-mass energy of 14 TeV. The experimental signatures of black hole formation in the ATLAS detector at the LHC are studied and compared with Standard Model (SM) backgrounds. Black holes can be produced by the large extra dimension model with black hole mass $M_{BH} = \sqrt{\hat{s}}$, where $\sqrt{\hat{s}}$ is the parton-parton Centre of Momentum System (CMS) energy squared. In the large extra dimension model, quantum gravity can become strong at a TeV energy scale in the bulk space-time, and could lead to microscopic black holes being produced and observed by the LHC experiments. Once black holes are produced in the collider, they will decay to the SM particles by Hawking evaporation. Under this scenario, an analysis was carried out to determine the significance of black hole signals above some SM backgrounds in the ATLAS detector. Five event selection criteria were applied to Monte Carlo black hole and background events. Consequently, the significance of the black hole and background events was far larger than 5σ. However, we did not include all SM backgrounds in this thesis.

Preface

The purpose of this thesis is to estimate the discovery potential for microscopic black holes in the ATLAS (A Toroidal LHC ApparatuS) detector. Before the LHC starts running, we have conducted an analysis for microscopic black hole events with a total luminosity of 10 fb^{-1} of LHC data. The analysis was based on the ATLAS detector and ATHENA software framework version 12.0.6. Since the LHC has not started yet, simulated and reconstructed Monte Carlo data were used for the data samples of signals and backgounds.

Black holes will be produced at the LHC if the large extra dimensions scenario by Arkani-Hamed, Dimopoulos and Dvali (ADD model) is valid. In the ADD model, the Standard Model particles and forces are confined to a 3-brane while gravity can propagate in the large size of extra dimensions, called the bulk. This provides the reason why gravity is weaker than the three other interactions on the 3-brane, and it also supports the grand unification theory by solving the hierarchy problem. Thus, we will discuss the theoretical models for black hole production at ATLAS in Chapter 1.

The LHC will be operated with centre-of-mass energy of 14 TeV with instantaneous luminosity $10^{34}cm^{-2}s^{-1}$. It is important to understand the structure of the ATLAS detector in order to understand the software and algorithms. Thus, in Chapter 2, there is information about the ATLAS detector with figures. The analysis was done within the ATHENA framework, so in Chapter 3 we will describe the process of the ATHENA framework. Chapter 4 describes a study of the discovery potential of black holes at ATLAS

with isolation cuts in order to identify and reconstruct particle objects in ATLAS software. In Chapter 5, we will briefly talk about the conclusion of the discovery potential for black hole events in the ATLAS detector.

Contents

List of Tables

List of Figures

Chapter 1

Theoretical background

1.1 The motivation of extra dimension models

1.1.1 The Standard Model

Physicists have been attempting to find the fundamental particles and interactions. Until now, our most accurate theory of fundamental building blocks of matter and interactions is the Standard Model (SM) which has been tested in many aspects. A number of the parameters and predictions in the SM have been verified experimentally. Although the SM of particle physics has been remarkably successful, the theoretical structure is not satisfactory since there are many unexplained parameters in it. However, it is well understood as an effective theory in the low energy regime, but it needs some fundamental theory beyond it to fulfill the picture of nature. Therefore, it is believed that there is *Beyond Standard Model* physics, or *new physics*, which gives motivation for high energy particle physics experiments such as ATLAS and CMS at the Large Hadron Collider (LHC) at CERN.[1]

[1] Centre Européen pour la Recherche Nucléaire on the border of France and Switzerland.

One can categorize the fundamental particles into two different types in the SM. One is the spin half fermions such as the three generations of *leptons* and *quarks*. The other particles in the SM are the spin one gauge bosons which mediate the fundamental forces. All leptons participate in weak interaction. Except neutrinos, charged leptons carry electric charge -1 which means that they also participate in the electromagnetic interaction. Quarks carry non-integer electric charge and colour charge − red, blue, and green, so they participate in electromagnetic, weak, and strong interactions. All matter consist of fermions, and their masses arise from interaction with the spin zero Standard Model *Higgs boson*, which gives mass to fermions and gauge bosons under the spontaneous symmetry breaking of the $SU(2)_L \times U(1)_Y$ gauge group in the SM. The Standard Model Higgs boson is the only SM particle which has not yet been discovered experimentally. Four experiments of the Large Electron Positron collider (LEP)[2] at CERN have determined the lower bound on the Standard Model Higgs boson mass of $m_h > 114.4$ GeV[3] [1]. Thus, one of the main objectives of the LHC is to discover the SM Higgs boson or Higgs bosons in new physics.

The fundamental forces in the SM are the electromagnetic, the weak, and the strong forces. The forces are expressed as the quantum mediators with various masses, which are exchanged between fundamental particles. For example, the massless *photon* transmits the electromagnetic force. The weak force can be explained by the massive mediators the Z^0, mass of 95 ± 3 GeV, and $W^{\pm}$, mass of 81 ± 5 GeV. The massless *gluons* are interacting among the color charged particles (the quarks and gluons) at the short range of $\approx 10^{-15}$m. Due to the colour confinement, there is no evidence of a colour singlet in the SM. The weak interaction was first discovered in β decay from nuclear experiments. It allows the quarks to change their flavors in the SM due to the coupling of W boson to the quarks. Although the gravitational force is important to fulfil the whole picture of nature, it is not included in the SM. Table 1.1 summarises the four fundamental forces with mediators in nature.

[2]The Large Electron Positron collider before the LHC.

[3]$\hbar = c = 1$ in natural units which are used throughout unless otherwise indicated.

Force	Range (m)	Strength	Mediator	Coupling constant
Electromagnetic	Infinite	$\frac{1}{137}$	Photon	α_1
Weak	$\sim 10^{-18}$	10^{-6}	$W^{\pm}$, Z^0	α_2
Strong	$\sim 10^{-15}$	1	Gluons	α_3
Gravitational	Infinite	10^{-39}	Graviton	-

Table 1.1: The fundamental forces in nature. (The gravitational force is not included in the SM).

In addition the fermionic particles of the SM are summarised with various quantum numbers in Tables 1.2 and 1.3. The quantum numbers for isospin (I) and the third component of isospin (I_3) are different for the left and right-handed fermions, and the gauge field only couples to left-handed fermions. The weak isospin symmetry is often referred to as $SU(2)_L$. Thus the quantum numbers in the tables only refer to left-handed states. Even though neutrino mass oscillation was observed at several places lately [2], the neutrinos are treated as massless particles, and only left-handed neutrinos exist in the SM. The hypercharge (Y) which is related to electric charge (Q) and the third component of isospin (I_3) is defined as $Q = Y/2 + I_3$ by the Gell-Mann-Nishijima formula.

There are two further conservation numbers − lepton number L and baryon number B − in all the terms in the Lagrangian. Lepton number +1 is for leptons, and -1 is for anti-leptons. Any other particles have lepton number zero. In the case of baryon number, quarks have baryon number +1/3, and anti-quarks have -1/3 which means that baryons have $B = 1$. Other particles have baryon number zero. B and L are not given by the SM, but they appear to explain a symmetry in nature.

Leptons					
Name	Mass	Charge	Isospin		Hypercharge
l	(MeV)	(Q)	(I)	(I_3)	(Y)
electron(e)	~ 0.511	-1	$\frac{1}{2}$	$-\frac{1}{2}$	-1
ν_e	0	0		$\frac{1}{2}$	
muon(μ)	~ 105.658	-1	$\frac{1}{2}$	$-\frac{1}{2}$	-1
ν_μ	0	0		$\frac{1}{2}$	
tau(τ)	~ 1776.990	-1	$\frac{1}{2}$	$-\frac{1}{2}$	-1
ν_τ	0	0		$\frac{1}{2}$	

Table 1.2: Lepton content in the SM with relevant quantum numbers. Neutrinos are considered as massless in the SM.

Quarks					
Name	Mass	Charge	Isospin		Hypercharge
q	(MeV)	(Q)	(I)	(I_3)	(Y)
up (u)	$1.5 \sim 3.0$	$\frac{2}{3}$	$\frac{1}{2}$	$\frac{1}{2}$	$\frac{1}{3}$
down (d)	$3.0 \sim 7.0$	$-\frac{1}{3}$		$-\frac{1}{2}$	
charm (c)	1250 ± 90	$\frac{2}{3}$	$\frac{1}{2}$	$\frac{1}{2}$	$\frac{1}{3}$
strange (s)	95 ± 25	$-\frac{1}{3}$		$-\frac{1}{2}$	
top (t)	174200 ± 33	$\frac{2}{3}$	$\frac{1}{2}$	$\frac{1}{2}$	$\frac{1}{3}$
bottom (b)	4200 ± 70	$-\frac{1}{3}$		$-\frac{1}{2}$	

Table 1.3: Quark content in the SM with relevant quantum numbers. These data are based on PDG (Particle Data Group) 2006 information.

James Clerk Maxwell gave a big inspiration to the unification of the forces when he combined electricity and magnetism into electromagnetism. Einstein also had a picture of combining gravity with the electromagnetic force in a unified field theory of general relativity though Einstein's idea was not successful [3]. Abdus Salam, Sheldon Glashow and Steven Weinberg (GWS) succeeded to combine the weak and electromagnetic forces, the so-called electroweak force, at the energy scale of $\sim 10^3$ (GeV) by 1969 [4] [5]. As previously mentioned, there are three massive intermediate vector bosons. Two of them are charged ($W^{\pm}$), and one is neutral (Z^0). Their masses were reported by UA1 and UA2 at a proton-antiproton collider, CERN in 1983 [6] [7]. These experimental results supported predictions of the electroweak interaction and fundamental aspects of the Standard Model.

For the next step, how can we combine the electroweak force with the strong force? Sheldon Glashow and Howard Georgi proposed the Grand Unification Theory (GUT), which combined the three gauge groups $SU(3)_C \times SU(2)_L \times U(1)_Y$ into a single gauge group $SU(5)$ symmetry [8]. It places the quarks and the leptons in a large single symmetry group $SU(5)$ so that a quark can convert into a lepton. It means that baryon number conservation is violated, and the proton is not completely stable and decays into a pion and a lepton via an X or Y boson.

Under the Grand Unification Theory, all fundamental forces merge into one force to describe the existance of everything. Nevertheless, there is one very important problem in the SM. That is the hierarchy problem. It is caused by the different energy scales between the electroweak scale and the GUTs scale. As it is illustrated by Figure 1.1, the running couplings with energy scale do not exactly converge at a high energy scale around 10^{15} GeV in the SM [9]. The strong coupling α_3 which is related to $SU(3)_c$ is decreasing at very short distance because of the anti-screening effect. On the other hand, the electroweak coupling constants α_1 and α_2 which are related to $U(1)_Y$ and $SU(2)_L$ are increasing at short distances.

Now, the question is how could one make them converge to a single point around 10^{15} GeV. The hierarchy problem in the SM is one of the motivations

for searching for new particles or new physics which will modify the running couplings into a single value. Accordingly, SUSY (Supersymmetry) and extra dimension models motivated by string theory can be the solution for this vexing problem in the SM. Their ideas are different, but they have the same aim, namely solving the hierarchy problem. This will be discussed in the next sections.

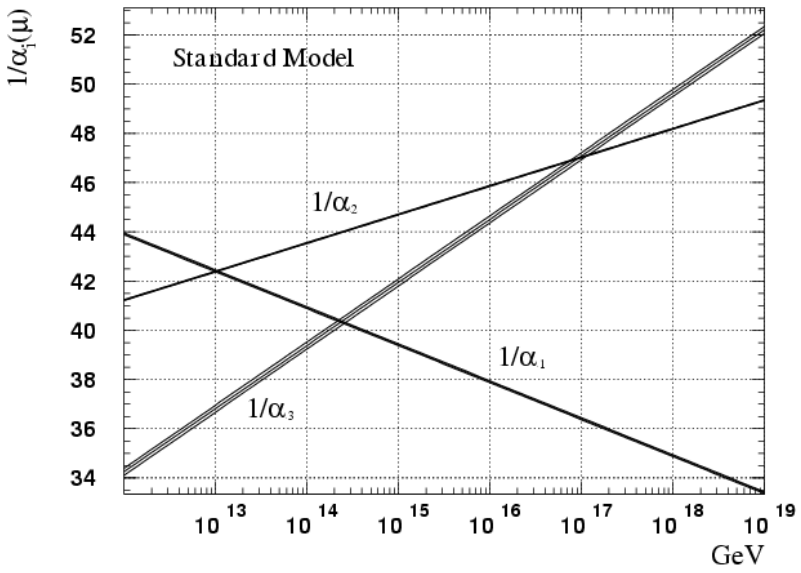

Figure 1.1: The gauge 'running' couplings with energy scale at high energy. One-loop evolution of the gauge couplings in the SM. Where $1/\alpha_1$, $1/\alpha_2$, and $1/\alpha_3$ correspond to the electromagnetic, the weak, and the strong couplings respectively. (Reproduced from ref. [10]).

The Standard Model of particle physics is well understood as an effective theory at a relatively low energy regime (the electorweak interaction) with presently available experimental data. However, the theoretical structure is not satisfactory in that there are many *ad-hoc* numbers, and the gravitational force is not included in it to fulfill a whole picture of nature. Furthermore, the prominent questions in the SM are

- There is no symmetry which relates the three independent gauge couplings in the SM.

- Are quarks and leptons somehow related? Why are fermions organized in the (rather *ad-hoc*) pattern of right-handed singlets and left-handed doublets?
- Why do the fermions have three generations?
- Why is electric charge quantized, and what explains the relations between the charges of fermions?
- Why is gravity so much weaker than the other forces and not included in the SM physics?
- There is no dark matter candidate in the SM.

These questions cannot be answered by the Standard Model. Hence, there should be some fundamental theory beyond the Standard Model, which is referred to as *new physics*, at a high energy regime. Fortunately, there are various theoretical postulations which may give us an answer for beyond the Standard Model physics. In order to discover the missing particle (Higgs boson) in the SM and to describe the new physics, it was necessary for particle physicists to build the Large Hadron Collider in the LEP tunnel at CERN.

1.1.2 Hierarchy problem

One of the most vexing problems of the SM is the hierarchy problem. It arises in the separation between the electroweak and the GUT scale. The electroweak symmetry breaking scale of the order of $(\sqrt{2}G_F)^{-1/2} \approx 246$ GeV is provided by the Higgs mechanism, while a unification of all three gauge couplings is on the order of the grand unification scale $\sim (10^{14} - 10^{16})$ GeV. If the new physics sets in at the GUT scale, then the SM should be valid from the vacuum expectation value of the Higgs (VEV)=$(\sqrt{2}G_F)^{-1/2} \approx 246$ GeV to M_{GUT}, which leads to a fine-tuning of the free model parameters to around one part in $10^{24} - 10^{28}$ GeV. As long as the energy difference between

the two associated symmetry ($SU(2)_L \times U(1)_Y$ and GUT) breaking scales becomes large, fine-tuning is needed to resolve the hierarchy problem with some symmetry relating the various parameters in the high energy region. Since there is, however, no symmetry relating the various couplings in the SM, fine-tuning is very unnatural [11].

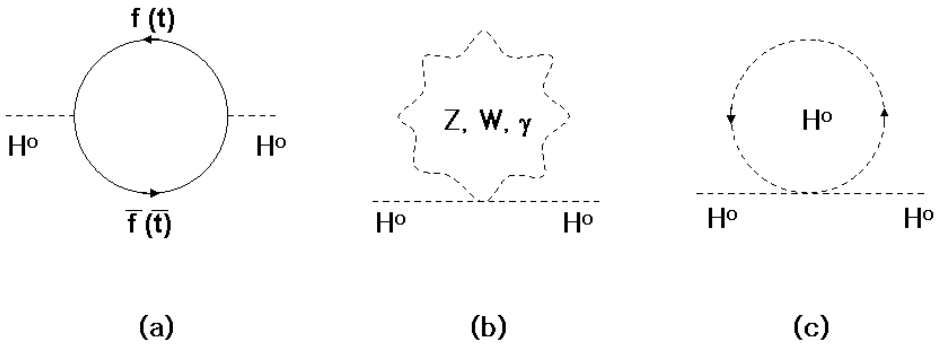

Figure 1.2: The one-loop correction to the Higgs mass in the Standard Model. (a) Higgs coupling to fermions (b) Higgs coupling to gauge bosons (c) Higgs coupling to itself.

Technically, the hierarchy problem arises from the quantum correction of the Higgs boson mass at high energy, which is quadratically divergent mainly due to the tadpole diagram involving Higgs self-interaction. An extreme fine-tuning within the framework of the SM is needed in order to stabilize the Higgs boson mass at high energy.

Experimentally, the electroweak fit gives the lower bound on the physical Higgs mass $m_h < 219$ GeV with 95% CL at LEP and SLC[4] [12]. The Higgs mass parameter ${m_H}^2$ contains the uncalculable cut-off (Λ) dependent quantum corrections. The following equation is the correction to the Higgs mass from the Higgs coupling to a fermion

[4]Stanford Linear Collider.

$$\delta {m_H}^2 = \frac{|\lambda_f|^2}{16\pi^2}\left[-2\Lambda^2 + 6{m_f}^2 \ln\left(\frac{\Lambda}{m_f}\right) + \cdots\right], \tag{1.1}$$

where λ_f is the coupling of Higgs-fermion, and m_f is the fermion mass. For new physics above the Λ scale, it is possible to expect that the Higgs mass parameter can be at least the size of Λ which will stabilize the range of the Higgs mass to solve the hierarchy problem. If one can assume that the SM is valid up to a scale $\Lambda = 10$ TeV, $\delta {m_H}^2$ from the leading quadratically divergent correction to Higgs mass are:

$$Top\ loop \quad : \quad -\frac{3}{8\pi^2}{\lambda_t}^2\Lambda^2 \quad \sim \quad -(2\ TeV)^2 \tag{1.2}$$

$$Gauge\ loop \quad : \quad \frac{1}{16\pi^2}g^2\Lambda^2 \quad \sim \quad (0.7\ TeV)^2 \tag{1.3}$$

$$Higgs\ loop \quad : \quad \frac{1}{16\pi^2}\lambda^2\Lambda^2 \quad \sim \quad (0.5\ TeV)^2. \tag{1.4}$$

Without considering tuning, the cut-off is rather low

$$\Lambda < 600\left(\frac{m_h}{200\ \text{GeV}}\right)\ \text{GeV}. \tag{1.5}$$

If we assume that the valid energy range of the SM is up to $\Lambda = 100$ TeV, the fine-tuning is about one part in 10000. On the other hand, if the cut-off is around $\Lambda = 1$ TeV, the requirement for fine-tuning will disappear completely. If there is a Standard Model Higgs boson, and the fine-tuning is unnatural, there must be new physics at an energy scale $\Lambda = 1$ TeV to contribute to the Higgs mass [13] [14].

In order to solve the hierarchy problem for physics beyond the SM, supersymmetry (SUSY) and extra dimensions are the most well developed theoretical models. The fundamental idea of SUSY is there is a symmetry between fermions and bosons. It also provides the unification of three fundamental interactions and gravity around the Planck scale, $M_P \approx 10^{19}$ GeV. In particular, supersymmetry can give an answer to the hierarchy problem of energy scales from the electroweak scale to the Planck scale. There is no unification of gauge couplings in the SM, but it is possible to achieve it in the minimal supersymmetry of the SM (MSSM), which consists of taking the SM and adding

the corresponding supersymmetric partners. Figure 1.3 shows the unification of gauge couplings in SUSY model.

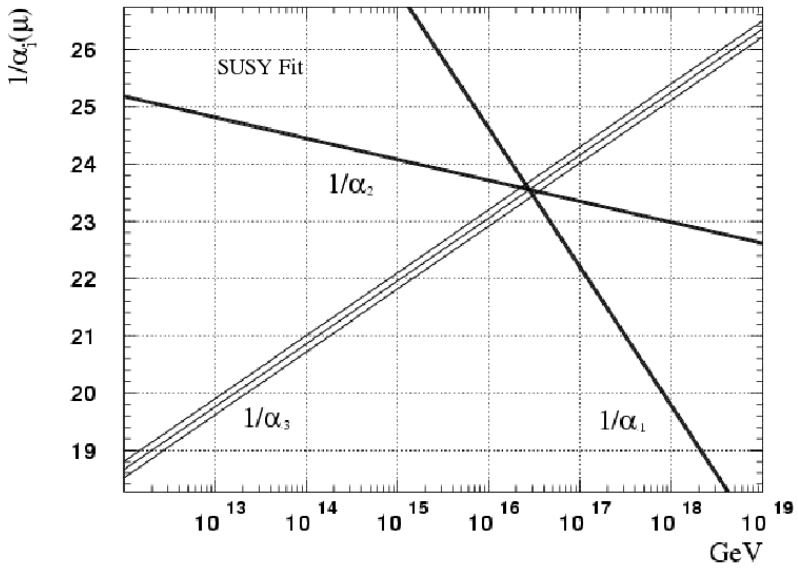

Figure 1.3: The gauge 'running' couplings with energy scale at high energy. One-loop evolution of the gauge couplings in SUSY. (Reproduced from [10]).

1.2 Extra dimensions

Extra dimension models are novel model-building phenomenologies used directly or indirectly to explain the large separation between the three interactions in the SM and gravity, that is, the hierarchy problem. Kaluza and Klein (KK-theory) in the early 1920s attempted to unify electromagnetism and gravity by extending general relativity into five dimensional spacetime. This is the earliest extra dimension model to combine gravity with electromagnetism. It was not popular for a long time since it failed to explain the weak and strong interactions and the weakness of gravity. Recently, string theory has brought up extra dimension models as a method of solving the hierarchy problem, SUSY breaking, the fermion mass hierachy, and the neutrino mass spectrum.

The Planck scale ($\sim 10^{19}$ GeV) is the energy scale where gravity becomes comparable to the gauge interactions in the SM. Referring to Table 1.1, our knowledge of the weak and strong interactions can describe a range of order $\sim 10^{-15}$ mm, and the gravitational interaction is easy to ignore by the fact that it is very weak at a long distance. Moreover, we have no experimental data in the gravitational interaction in a range of ~ 1 mm. Thus it is possible that gravity at a smaller distance than a millimeter may have different characteristics from the 3-dimensional Newtonian theory. Meanwhile, some of the extra dimension models allow the SM particles such as bosons, fermions, and gauge fields to be localised on the 3-brane, where we live while the gravitational force propagates into the bulk, the so-called extra dimensions. Hence, the propagation of gravity into the bulk becomes a very important issue among extra dimension models because it can explain why gravity is relatively weaker than the three other gauge interactions.

Different extra dimension models have different phenomenologies. However, all the models are related to the following postulates.

- The 3-spatial subspace dimensions in which we live are known as the '3-brane' or 'membrane', and this brane is embeded in extra dimensions, $D \equiv (4+n)$, where D is the total number of dimensions, and n is the number of extra dimensions.

- The important idea of extra dimension models is the explanation of the weakness of gravity to solve the hierarchy problem in the SM. There are different ways of solving this problem, but in general, gravity propagates in the extra dimensions; known as the *'bulk'*, and other gauge interactions and particles in the SM are confined on the 3-brane. Namely, gravity is weak on the 3-brane because it propagates into extra dimensions.

- n are compactified on a circle of radius R the so-called compactification radius. All propagated fields in the extra dimensions are Fourier expanded into a complete set of modes − the KK tower of states. All

fields which propagate into the bulk can be compared to particles in a box. There are the n-compactified dimensions, and the momentum of the field in the bulk is quantized.

We can consider the geometry of the full $(4 + n)$-dimensional space time with metric tensor G_{IJ}, where the 4 and n dimensional geometries are independent. The metric G_{IJ} in the factorized case can be expressed in the following form

$$ds^2 = G_{IJ}dx^I dx^J = \eta_{\mu\nu}dx^\mu dx^\nu + h_{ij}(y)dy^i dy^j, \tag{1.6}$$

where x^μ are coordinates for the four dimensions, and y^i are coordinates for the extra compact space, where $I, J = (0, \cdots, 3 + n)$, $\mu, \nu = (0, \cdots, 3)$ and $i, j = (1, \cdots, n)$. $\eta_{\mu\nu}$ is the metric tensor of 4-dimensional space time, and s is a distance of a geodesic line in a $(4+n)$ dimensional space. The metric h_{ij} describes the extra dimensions as *flat* only if they are toroidal, as assumed in the Arkani-Hamed, Dimopoulos, and Dvali (ADD) extra dimension model [15] [16]. If the metric G_{IJ} is non-factorizable, there is a function of y factor multiplying $\eta_{\mu\nu}dx^\mu dx^\nu$, which means the bulk geometry is naturally curved. This is referred to as *Warped extra dimensions*. The simplest form of the Warped extra dimensions model is known as the RS (Randall and Sundrum) extra dimensions model [17] [18]. So far, these are general features of extra dimension models. In addition extra dimension models have been developed recently to explain and understand how extra dimensions can help to solve the hierarchy problem, and how they can manifest themselves in particle physics. There are three popular models, and we will discuss them in the next section.

1.2.1 Different extra dimension models

The Large Extra Dimensions (ADD model)

There are three distinct extra dimension models at the TeV scale with different phenomenologies. An early extra dimension model is the ADD (Arkani-Hamed, Dimopoulos and Dvali) model or *Large Extra Dimensions*. In this model, only gravity can propagate in the bulk but not the SM particles. In other words, gravity in ADD models at long distances within the 3-brane is diluted because it propagates in the bulk while the SM particles and interactions are on the 3-brane. If the volume of the compactified n-additional dimensions is V_n, the relation between the fundamental scale $\overline{M}_D$ and the reduced Planck scale, $\overline{M}_P$ is [15] [16]

$$\overline{M}_P{}^2 = V_n \overline{M}_D{}^{2+n}. \tag{1.7}$$

In the ADD model, the extra dimensions are *flat* and compactified in toroidal form. If $\overline{M}_P \sim 1$ TeV, there is no longer a fine-tuning and the hierarchy problem between $\overline{M}_P$ and the electroweak scale which means that the fundamental scale of gravity can be as low as the electroweak scale, and this is low enough to be detected at the LHC. If all radii are of equal size R, we can define $V_n = (2\pi R)^n$ where R is smaller than a millimeter for $n = 2-6$. For an additional dimension $n = 1$, Newton's law is still valid on solar-system scales. While the large size of the extra dimensions forces the SM fields to be confined to the 3-brane, the bulk graviton propagates as a KK tower where $\vec{n}$ labels the KK excitation level. To test extra dimensions in a high energy collider, we can directly or indirectly measure KK gravitons as jets and missing energy.

There are two main experimental signatures in colliders. One is the direct production of the KK states of bulk gravitons (G_n) which will appear as jets and missing transverse energy: $pp \to jet + \not{E}_T$ at the LHC from the subprocesses $qg \to qG_n$, $q\bar{q} \to gG_n$, and $gg \to gG_n$. If the KK graviton is observed at a detector, then both parameters $\overline{M}_D$ and n can be determined by measuring the production rate at different values of $\sqrt{\hat{s}}$. The other one is a virtual KK graviton (bulk graviton) exchange at tree-level in the $2 \to 2$ scattering.

The production of black holes at the LHC is based on large extra dimension models [19].

$\mathbf{TeV^{-1}}$-sized Extra Dimensions

Second of all, there are $TeV^{-1} - sized\ Extra\ Dimensions$, and this model is rather different from the large extra dimensions and warped extra dimensions in RS models. The feature of this model is the small size of the extra dimensions, so some of the SM gauge fields and Higgs bosons can be present in the bulk or on the brane. The SM fermions are also confined to the brane or to a specific area of the extra dimensions. Thus, the small volume of the bulk in this model is not large enough to explain why gravity is weak on the 3-brane, and there is also still the hierarchy problem.

If Higgs bosons propagate in the bulk, the vacuum expectation value of the Higgs zero-mode is able to generate spontaneous symmetry breaking. One more useful motivation for TeV^{-1}-sized extra dimensions is the three generations of fermions. In this model, there are two branes in the TeV^{-1}-sized extra dimensions, and they are separated by a TeV^{-1}. Thus, there is the possibility to suppress proton decay if the quarks are localized on one brane and the leptons on the other [20].

Warped Extra Dimensions (RS model)

Warped extra dimensions solve the hierarchy problem but in a different way from the large extra dimension models. The difference is that gravity is not diluted by the large extra dimensions but by the curvature of extra dimensions. In this model, a product of four dimensions and extra dimensional compact space become the higher-dimensional spacetime. Thus, the metric is nonfactorizable from equation (1.6), and it can be expressed as follows

$$ds^2 = e^{-2ky}\eta_{\mu\nu}dx^\mu dx^\nu - dy^2, \tag{1.8}$$

where k is a scale of the order of the Planck scale, which describes the curvature of the extra space, and $y = r_c\phi$, where $0 \leq \phi \leq \pi$ is the coordinate for the

extra dimension, whereas r_c is the size which sets up a finite interval between the 3-brane and warped extra dimensions, and it is not neccessary to be large, which means extra dimensions are small compared with ADD model. While the SM particles are set on the 3-brane, gravity is on the other brane, which is multiplied by a warp factor. That is why gravity in the 3-brane is weak, but it is strong in warped extra dimensions. The RS model can also explain why the cosmological constant is small [17] [18].

1.3 Black hole production at the LHC

The extra dimension models were introduced in section 1.2. Among the three different models, the large extra dimension model (ADD model) and Warped extra dimension model (RS model) allow a solution to the hierarchy problem. In this thesis, black hole production at the LHC will be studied within the frame work of the ADD model. From equation (1.7), we can derive the relationship between the Planck scale and the fundamental scale $\overline{M}_D$. The volume of extra dimensions will determine the two scales in the ADD model. However, the Planck scale, $M_{P(4)} \sim {G_{(4)}}^{-1/2}$, can be deriven from Einstein's field equation and the Schwarzschild solution for the metric of spacetime, where G is the Newtonian gravitational constant. Initially we follow the ADD conventions using Gauss' law in extra dimensions, so the Planck scale in $(4+n)$ dimension is written as [14]

$$M_{P(4+n)}^{n+2} = \frac{1}{4\pi G_{(4+n)}} \frac{1}{R^n}, \tag{1.9}$$

where R is the compactified radius and $G_{(4+n)}$ is the gravitational constant in $(4+n)$ dimension.

If the number of extra dimensions $n = 1$ and the Planck scale is about 1 TeV, one can obtain a very large size for extra dimensions of approximately 10^{11} m, which can be ruled out. In the case of $n = 2$, the size of extra dimensions will be about 0.67 mm. The Newtonian gravitational force will also transition from $1/r^2$ to $1/r^4$, and it might not behave as Newtonian gravitation, which is well understood at a distance of ~ 1 mm.

Karl Schwarzschild obtained the Schwarzschild radius R_S of black holes by applying general relativity to a static non-spinning massive object. If an object has mass M and radius r, the Schwarzschild radius is $R_S = 2G_{(4)}M/c^2$. The Schwarzschild radius of the earth is approximately 1 cm which means $R_S \ll r$, and the earth is not a black hole.

In order to find experimental evdience of extra dimensions and to produce black holes, the black hole mass M_{BH} must be far larger than the fundamental Planck scale $M_{P(4+n)} \sim$ TeV so that black holes can be well understood according to general relativity. In addition, the production of black holes will be treated as a classical process.

First of all, the Schwarzschild radius R_S (event horizon) of the black hole in (4+n) dimensions is given by [21]

$$R_s = \frac{1}{\sqrt{\pi} M_{P(4+n)}} \left[\frac{M_{BH}}{M_{P(4+n)}} \left(\frac{8\Gamma\left(\frac{n+3}{2}\right)}{n+2} \right) \right]^{\frac{1}{n+1}}. \tag{1.10}$$

Where M_{BH} is the mass of the black hole and M_P is the Planck scale in the total number of dimension. At the LHC, the centre-of-mass energy is $\sqrt{s} =$ 14 TeV, and protons from opposite directions will collide at the interaction points. If we consider $\sqrt{\hat{s}} = M_{BH}$, and the impact parameter is smaller than the Schwarzschild radius, black holes can be produced at the LHC. Therefore, the total cross section in the classical approximation can be estimated to be [22] [23]

$$\sigma(M_{BH}) \approx \pi R_S^2 = \frac{1}{M_{P(4+n)}^2} \left[\frac{M_{BH}}{M_{P(4+n)}} \left(\frac{8\Gamma\left(\frac{n+3}{2}\right)}{n+2} \right) \right]^{\frac{2}{n+1}}. \tag{1.11}$$

Classically, black holes only absorb and do not emit particles, but Hawking predicted that black holes can create and emit particles under quantum mechanical effects as black body radiation. The process is known as Hawking evaporation. Thus, the Hawking temperature T_H, which is proportional to the inverse of Schwarzschild radius is given by [14] [24]

$$T_H = \frac{\hbar c}{4\pi k R_S}. \tag{1.12}$$

Throughout Hawking evaporation, a black hole emits all kinds of particles, and its mass will decrease. Eventually, it will disappear. There are also many other

concerns about the decay of black holes and remnants. Hawking evaporation gives rise to experimentally observable signatures of black holes with high-multiplicity final states.

Consequently, if the black hole mass is $M_{BH} = \sqrt{\hat{s}}$, the impact parameter of partons from opposite directions is smaller than the Schwarzschild radius R_S in the ADD model, there is the possibility to produce black holes at the LHC. In this thesis, an analysis will be done under this scenario.

1.4 Experimental limits

Beside the production of micro black holes at the LHC, people also suspect that micro black holes can be produced in nature due to the interaction between ultra high-energy cosmic-ray neutrinos and the Earth's atmosphere. The Akeno Giant Shower Array (AGASA) has set a lower bound on M_D ranging from 1.0 to 1.8 TeV, for 4 to 7 extra dimensions at 95% confidence level [25]. It is expected that the Pierre Auger Observatory, which is an international cosmic ray experiment, will set more stringent limits during the first five years of operation.

The LEP experiments have investigated photons and missing energy in final states, and they have set experimental limits on M_D and n of 1.5 TeV for 2 extra dimensions to 0.75 TeV for 5 extra dimensions [26]. The CDF and DØ collaborations also search for final states of a monojet and missing energy, and the CDF collaboration set lower bounds with Run II data on M_D of 1.33 TeV for 2 extra dimensions to 0.88 TeV for 6 extra dimensions [27].

At present, experimental limits allow the fundamental scale of gravity to be as low as approximately 1 TeV. Accelerator experiments do not search for micro black holes directly but test the models by looking for the effect of bulk gravitons in extra dimensions. Thus, evidence of bulk graviton for extra dimension could allow us to determine the number of extra dimensions and the Planck scale.

Chapter 2

The LHC and the ATLAS detector

2.1 The Large Hadron Collider (LHC)

2.1.1 The layout of the LHC

The Large Hadron Collider (LHC) has been scheduled to begin operation in May 2008. At the end of 1996, the CERN council decided to build the LHC in the Large Electron Positron (LEP) collider tunnel with the centre-of-mass energy 14 TeV. The LHC is a proton-proton (pp) collider with nominal beam luminosity of 10^{34} cm^{2}s^{-1} [28].

The LHC is located about 100 m underground crossing the French and Swiss border. It has two-in-one superconducting magnets to lead the counter-rotating protons or heavy Pb ion beams in separate beam tubes. The collider is in the LEP tunnel with circumfrence of about 27 km.

The LHC aims to discover the Higgs boson and study rare events in the SM and beyond SM physics which requires high beam energies and high beam

intensities to discover them. In order to reach the TeV scale of center-of-mass energy, protons are accelerated in the LHC collider to an energy of 7 TeV.

There are several reasons why hadrons such as protons and lead ions are used for the LHC projectiles.

- In order to reach high energy collisions, massive particles have a strong advantage in a circular accelerator. Heavy particles such as hadrons loose far less energy per turn than light particles such as electrons in a collider. Thus, hadrons are better to achieve high energy collisions. In addition many magnets will be used to accelerate the beams, so charged hadrons are suitable for the LHC. As a result, protons have been chosen for the LHC projectiles.

- There are more advantages that protons will have as the LHC projectiles. Firstly producing protons is much easier than producing anti-protons. Secondly we can eliminate the process of storing anti-protons during pre-injection steps. That will allow us to obtain the high luminosity of the LHC.

- Protons consist of quarks, anti-quarks and gluons, and more types of interactions could occur in one pp hard collision than those in one point-particle point-particle collision such as electron-positron collision. Generally, hadron colliders are mainly used for discovering new particles, so the LHC needs to collide proton beams, though more QCD backgrounds are present in the collisions.

The layout of the LHC main ring is a series of eight arcs and straight regions. Insertions in eight straight sections, as shown in Figure 2.1, are about 528 m long. In four insertion regions the proton beams cross and collide at interaction points in the centre of the detectors. The other four insertions will be mainly operated for beam cleaning, beam dump system, and RF (Radio Frequency) and beam instrumentation.

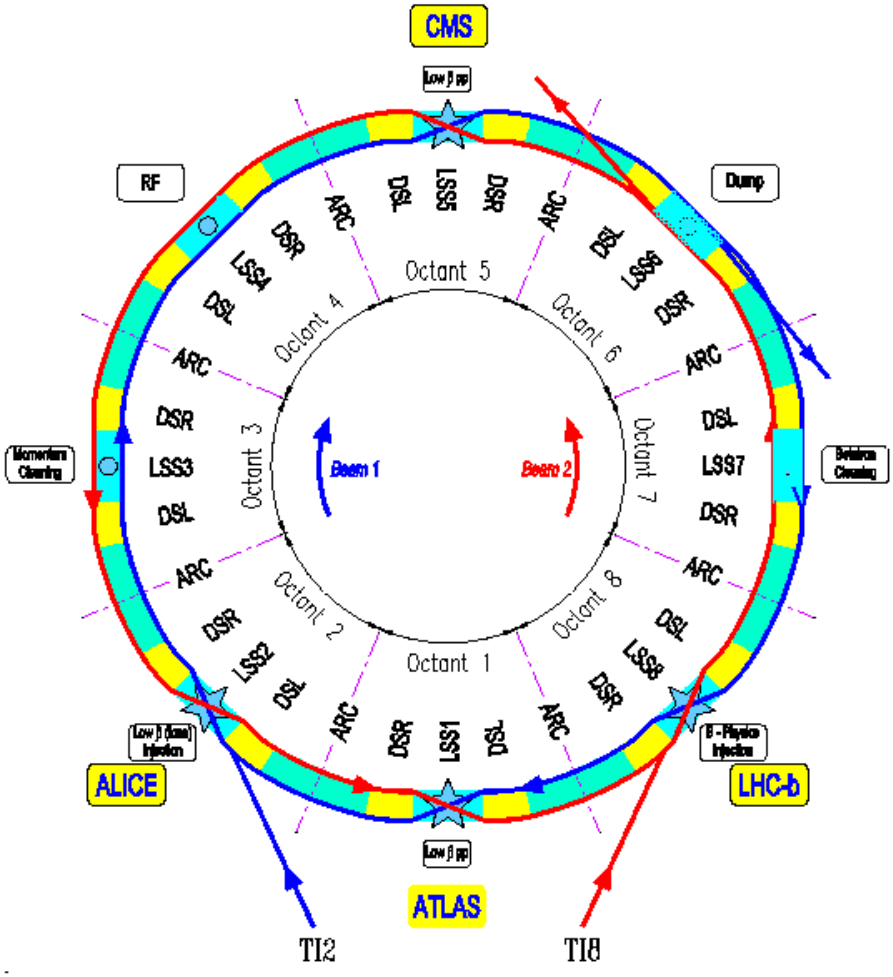

Figure 2.1: The layout of the LHC main ring.

The LHC has four separated interaction points (IPs). There are two high luminosity general purpose experiments, ATLAS (A Toroidal LHC ApparatuS) and CMS (Compact Muon Solenoid), aiming at a peak luminosity of 10^{34} cm^{-2}s^{-1}. They are designed to cover a wide range of physics such as confirmation of SM physics and the search for beyond standard model physics such as SUSY, extra dimensions, and micro black holes. TOTEM (TOTal Elastic and diffractive cross section Measurement) is installed with the CMS to measure the total cross section for elastic scattering and diffractions at small angles aiming at a peak luminosity of 2×10^{29} cm^{-2}s^{-1}. ALICE (A Large Ion Collider Experiment) is a heavy ion collision detector with a lower

peak luminosity of 10^{27} cm^{-2}s^{-1}. The LHCb is for b-physics study with a peak luminosity of $L = 10^{32}$ cm^{-2}s^{-1}. The number of events per second produced in the LHC collisions at the interaction points is

$$N_{event} = L\sigma, \tag{2.1}$$

where L is the machine specific luminosity and σ is the cross section for the physics process. In many aspects, building a high beam energy and high luminosity collider pushes the limits of technology. Therefore, keeping stringent beam parameters for safe a running mode is important, and Table 2.1 shows the main beam parameters of the LHC.

	Injection	Collison	Units
Proton energy	450	7000	[GeV]
Relativistic gamma	479.6	7461	
RMS bunch length	11.24	7.55	[cm]
RMS beam size	375.2	16.7	[μm]
Helium temperature	1.9		[K]
Highest luminosity	10^{34}		[cm^{-2}s^{-1}]
Luminosity lifetime	10		[h]
Dipole field at 7 TeV	8.33		[T]
Nominal bunch spacing	25		[ns]
Circulating beam current	0.582		[A]
Distance between beams (arc)	194		[mm]
Total crossing angle	285		[μrad]
Energy loss per turn/proton/7 TeV	6.7		[keV]
Number of protons/bunch	1.15×10^{11}		
Number of bunches/beam	2808		

Table 2.1: The main beam parameters at the LHC.

As shown in Figure 2.2, the LHC will be supplied with protons from the injector chain Linac2. They are then accelerated up to 1.4 GeV in the Proton Synchrotron Booster (PSB) and further accelerated up to 25 GeV in the Proton Synchrotron (PS). At last, the Super Proton Synchrotron (SPS) accelerates protons to 450 GeV at which point they are fed into the LHC main

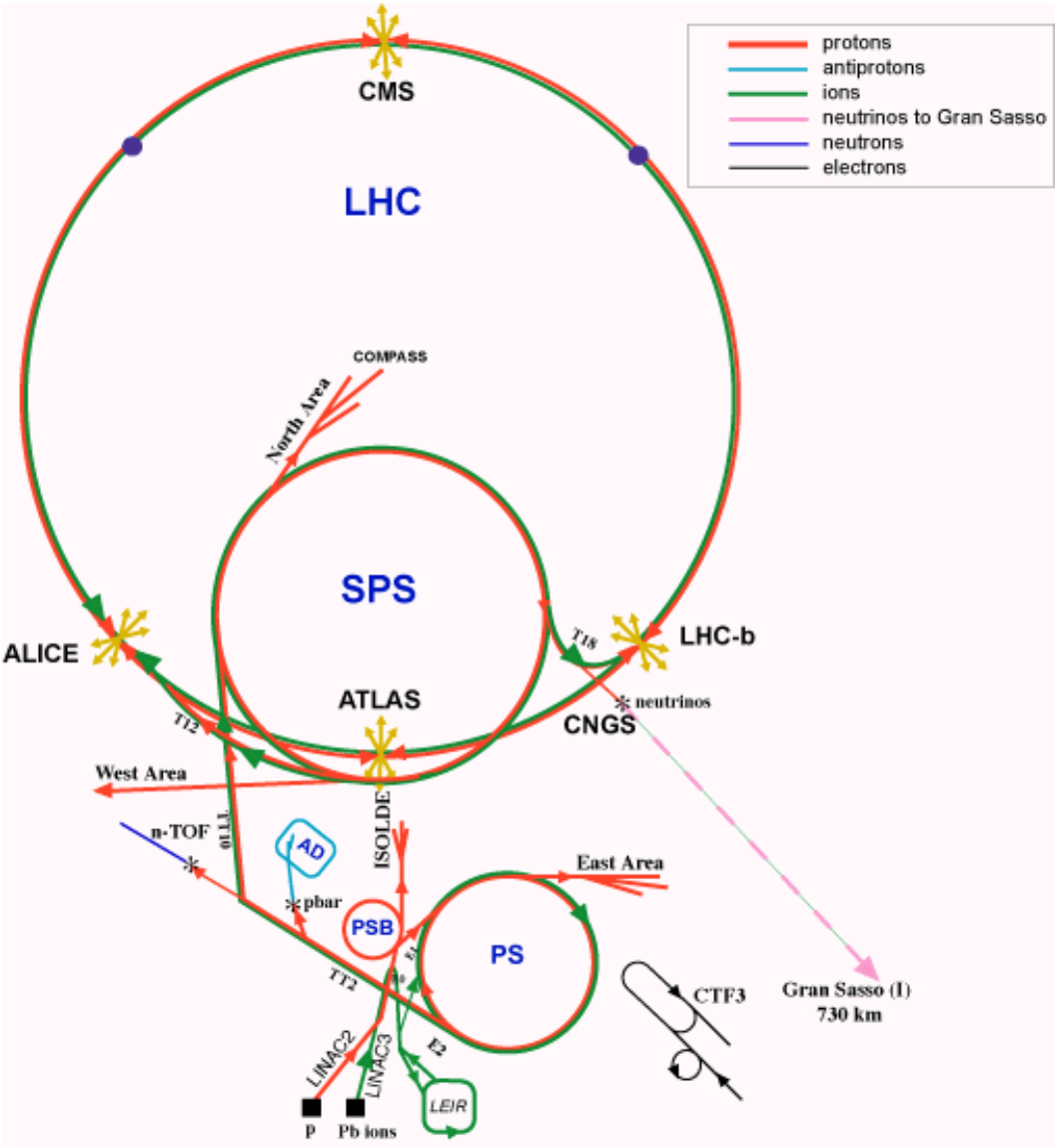

Figure 2.2: The LHC complex at CERN.

ring. As shown in Figure 2.2, a beam circulates clockwise and a beam counter-clockwise until each beam reaches 7 TeV in opposite directions.

2.1.2 Magnet system in the LHC

The LHC is appling superconducting technology for accelerator magnets to achieve proton-proton collisions at the center-of-mass energy of 14 TeV with a

nominal luminosity of 10^{34} $cm^{-2}s^{-1}$. The main dipoles and quadrupoles, which use superconducting Nb-Ti windings, operate in superfluid helium, and there are in total about 8000. Main superconducting dipoles for beam separation and recombination at the detectors can guide two equally charged protons in opposite directions by generating a magnetic field in the opposite sense in the two beam channels, and quadrupoles are mainly for focusing and defocusing the beams at the experimental insertions.

In addition to 1232 main dipoles at 8.33 T, 392 main quadrupoles are installed in the arc areas with gradients of 223 T/m. In the long straight sections, about 154 additional superconducting dipoles and quadrupoles are installed. Furthermore, thousands of smaller superconducting magnets are required for beam steering, correction of multipole errors, and so on. In the cleaning insertion areas, about 120 normal conducting magnets are installed in the LHC main ring, and more than 600 of them are installed in the SPS-LHC transfer lines. The LHC magnets operate in superfluid helium at 1.9 K, cooled by continuous heat exchange with flowing saturated superfluid helium [29].

2.2 The ATLAS detector at the LHC

The ATLAS (A Toroidal LHC ApparatuS) experiment is one of the four main experiments at the LHC. It is designed as a general purpose detector with detection of electrons, photons, muons, jets, and missing transverse energy as well as b-quark tagging. The overall layout of the ATLAS detector is shown in Figure 2.3.

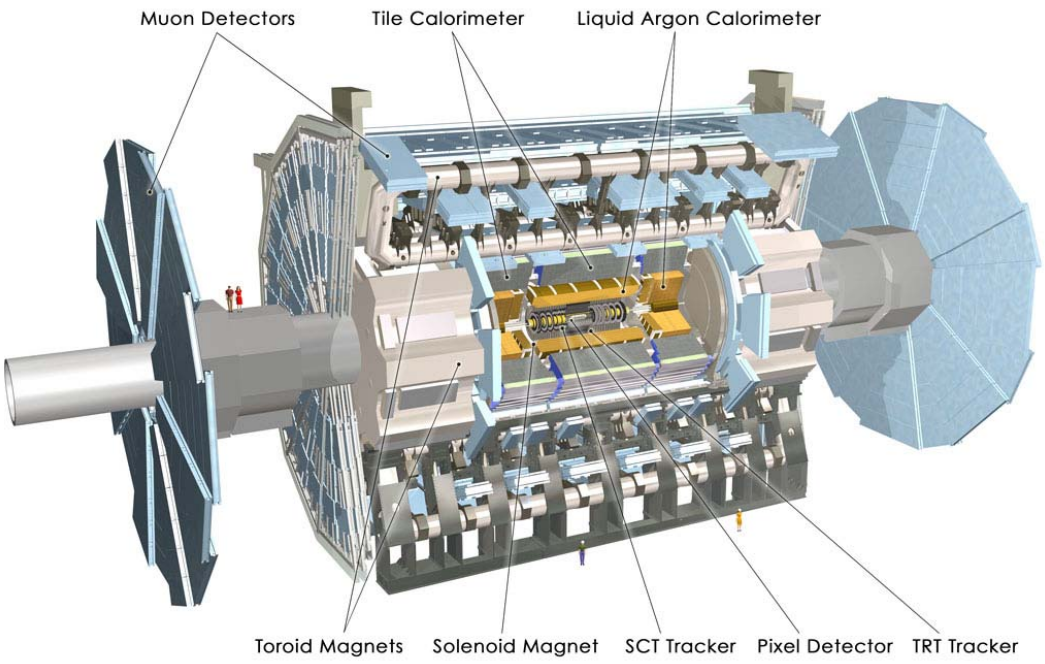

Figure 2.3: Overview of the ATLAS detector. The diameter is 26 m, and overall length is 46 m. The total weight of the ATLAS detector is about 7000 tons. The various subsystems are indicated.

The ATLAS detector is a large hybrid detector which has a basic geometry of layered cylinders that encompasses the collision point in the centre and four major layers: the inner detector, the electromagnetic calorimetry, the hadronic calorimetry, and the outermost muon spectrometer. The combined layers are used to track, identify or measure energy of certain produced particles after a collision. The magnetic system at ATLAS consists of an inner solenoid which surrounds the inner detector cavity, a large superconducting barrel toroidal magnet with an eight-fold symmetry outside the calorimeters, and two end-cap toroidal magnets outside the end-cap calorimeters.

At a luminosity of 10^{34} cm^{-2}s^{-1} there will be very large background rates especially QCD jets due to the nature of the proton proton collisions. In order to search for rare events among backgrounds, one has to understand signatures of particles in the detector. For examples, muons go through the detector without EM (electromagnetic) showering in the calorimetry, and they can easily be distinguished from jets. Electrons leave tracks in the inner detector and produce EM showers in the calorimetry. Good calorimetry and precise tracking systems with high granularity will allow us to identify electrons and photons and make E_T^{miss} measurements, which will rely on good measurements of EM shower energy and position over a wide acceptance range. However, the fine granularity becomes less important for the detector elements that are further away from the interaction point since the particle flux decrease as $1/R^2$.

The cylindrical structure of ATLAS allows the use of a cylindrical coordinate system. Thus, ATLAS requires large acceptance in *pseudorapidity* (η) with almost full azimuthal angle ϕ coverage. It is defined as

$$\eta = -\ln\left(\tan\frac{\theta}{2}\right) \ , \tag{2.2}$$

where θ is the polar angle, measured from the beam direction. The direction of the beam pipe is the z-axis, and the distance perpendicular to the z-axis is R. The azimuthal angle ϕ is used as in sperical coordinates in the x-y plane. Table 2.2 shows the purpose and η coverages of the ATLAS detector system [30] [31].

Detector component	Required resolution and characteristics	η coverage
Inner detector	$5 \times 10^{-4} p_T \oplus 1\%$ Enhanced electron identification τ-and b-tagging Secondary vertex detection at initial luminosities	± 2.5
EM calorimetry	$10\% \sqrt{E} \oplus 0.7\%$	± 3.2
Presampler detector	Enhanced $\gamma - \pi^0$ and γ-jet separation, direction measurements	± 2.4
Jet and $\not{E}_T$ Calorimetry barrel and end-cap forward	 $50\%/\sqrt{E} \oplus 3\%$ $100\%/\sqrt{E} \oplus 10\%$	 ± 3.2 $3.1 < \eta < 5.2$
Muon detection	10% at $p_T = 1$ TeV in stand-alone mode at highest luminosity	± 3

Table 2.2: General detector performance goals of ATLAS.

2.3 Inner detector

The Inner Detector (ID), as shown in Figure 2.4, is located closest to the beam pipe and is contained within a cylinder of length 6 m and a diameter of 2 m, in the central solenoidal magnetic field of 2 T [30] [32]. The inner detector consists of three important subdetectors: three cylindrical layers of Pixel detectors, four cylindrical layers of SemiConductor Tracker (SCT), and the Transition Radiation Tracker (TRT) in the outermost layer of the inner detector. The central solenoid is a length of 5.3 m and has a bore of 2.5 m. Due to the magnetic field in the inner detector, we can measure the momentum of the charged particles, by measuring the curvature of the tracks. The task of the inner detector is to reconstruct the tracks from charged particles and vertices in the event with high efficiency. The inner detector information on particles and vertices combined with the calorimeter and muon systems

information allows the reconstruction of an event.

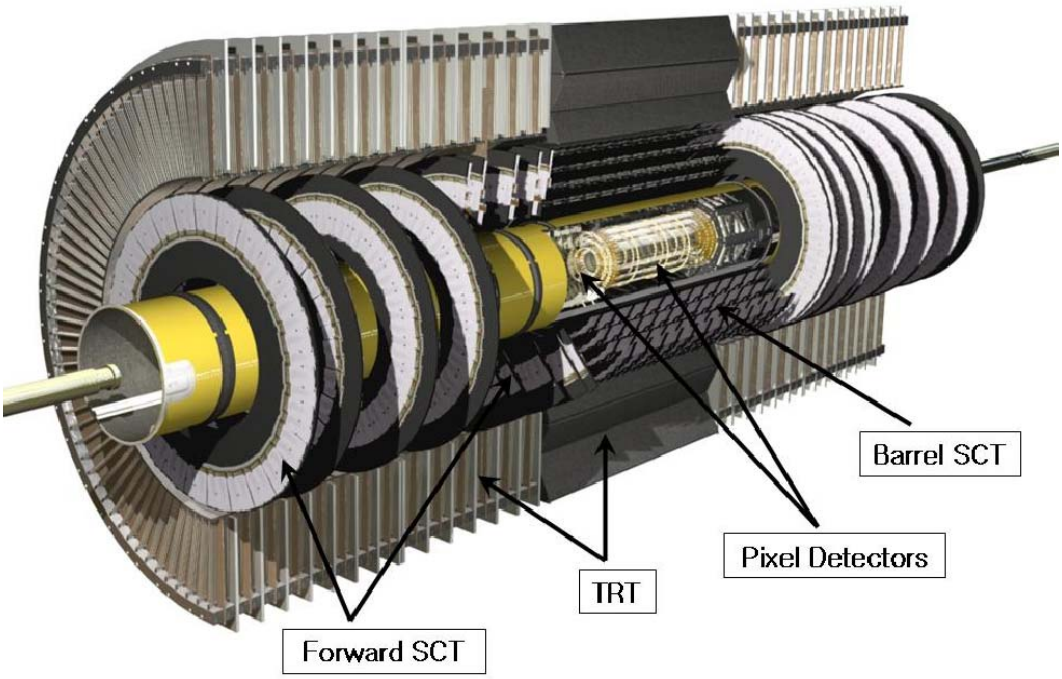

Figure 2.4: The ATLAS inner detector.

The pixel and SCT detectors are referred to as the high precision trackers with high granularity to measure the very large track density from the $p-p$ collisions at the IP. The pixel layers in the barrel region are at a radius of 5.05, 8.85, and 12.25 cm from the IP respectively, and there are three pixel disks on each side of forward region, with a total of 1744 modules. The area of the pixel sensor is 2×6 cm^2 and the thickness is 250 μm. In a module, there are 16 front-end chips and one module control chip. One front-end chip includes 160 rows and 18 columns of pixel cells, i.e. there are 2880 pixels per chip or 46080 pixels per module. Each pixel is 50 μm wide in $R-\phi$ and 400 μm long.

When a charged particle from the IP transverses the silicon sensor, it will produce free electron/hole pairs in silicon. If one applies a bias voltage, free charges will drift to the readout side of the sensor. In the readout electronics, a

discriminator determines the time over threshold (ToT) if the deposited charge is above threshold. The written out ToT information provides of the amount of charge that was deposited. In addition the pixel detector has over 80 million pixel cells. However, the high cost of precision layers gives the limitation of the total number of layers, and the pixel and silicon layers have been designed to be replaced because of the radiation damage from energetic particles with high luminosity.

The SCT system is at an intermediate radii in the inner detector. The SCT contains four complete barrels at radii of 300, 373, 447 and 520 mm, and the forward SCT are in three rings of nine wheels at distances between 835 mm and 2788 mm. The SCT in the barrel region contains 61 m^2 of silicon detectors with 6.2 million readout channels which are installed near the middle of the sensor. The SCT sensors are arranged parallel to the beam direction. The size of a silicon sensor is 6×12 cm^2, and there are 768 strips along the long side of sensor with width of 80 μm. One SCT module has two silicon sensors which are bound back-to-back by glue with a small relative angle of 40 mrad. Thus, one can measure a two dimensional space point by searching for the intersection of the two strips on the silicon sensors. If the tracks are separated by more than 200 μm, they can be distinguished. The SCT consists of about 6.2 million readout channels, and the spatial resolution is 16 μm and 580 μm in z direction. The continuous tracking sensers in the endcaps are wedge shaped into wheels. The SCT strips in this region are toward the beam pipe. On each end-cap region, there are nine SCT disks mounted with four modules on the each disk. The readout of the SCT modules is binary, and it depends on the hit rate. The pixels and SCT detectors cover the pseudorapidity region up to $|\eta| = 2.5$ while the TRT covers up to $|\eta| = 2.0$, and the acceptance of the inner detector covers $|\eta| < 2.5$.

The outermost layer, the Transition Radiation Tracker (TRT), contains ~ 36 layers of 4 mm diameter straw tubes with a resolution of ~ 200 μm, and it extends from a radius of 56 cm to 107 cm. There is a gold-plated tungsten wire in the middle of a straw. The TRT straws are filled with a gas mixture (70% Xe, 27% CO_2, and 3% O_2), and there are radiators between straws,

which emit transition radiation when an energetic electron passes through them. Also, if a charged particle passes through the straws, ionized clusters would be produced and drifted toward the tungsten wires so that the distances of the track of the charged particle from the wires are measured. Due to the large number of straws, the TRT can provide continuous tracking of charged particles. The barrel TRT straws are parallel to the beam pipe with 52,544 axial straws, and other end-cap trackers are located in planes perpendicular to the beam axis with 245,766 radial straws. Throughout the inner detector, impact parameter measurements, vertexing reconstruction, and pattern recognition will be performed over $|\eta| \leq 2.5$ [32].

2.3.1 Solenoid magnetic field

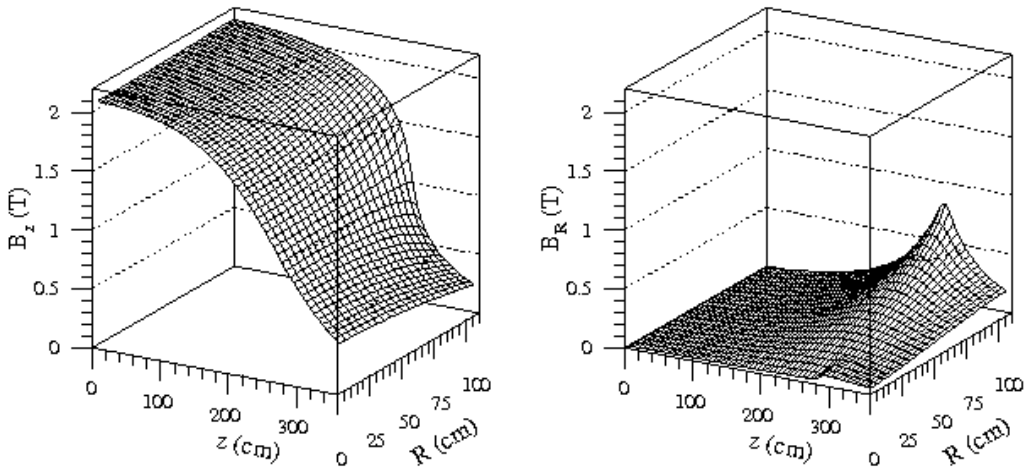

Figure 2.5: Left: The z component of the solenoid magnetic field in the Inner Detector, as a function of z and R. Right: The R component of the solenoid magnetic field, as a function of z and R [32].

Uniformity of the magnetic field is important for measuring the momentum of particles in the inner detector. However, there is a deviation of the field because the ATLAS solenoid is 5.3 m long, compared with the 6 m length of

the tracking volume of the inner detector. Figure 2.5 shows that uniformity of the magnetic field is broken in the forward region. The z component of magnetic field drops from 2 T to 1 T at the end of the inner detector, whereas the R component is up to 0.6 T in the forward region.

2.4 Calorimetry

The calorimetry of the ATLAS detecter consists of an electromagnetic calorimeter (EM), a hadronic calorimeter, and the forward calorimeter. The EM calorimeter and the hadronic calorimeter consist of the barrel region and identical end-cap regions on each side. The EM barrel calorimeter covers the pseudorapidity $|\eta| < 1.475$ and $1.375 < |\eta| < 3.2$ in the end-cap region, and hadronic barrel calorimeter covers $|\eta| < 1.7$ and the hadronic end-cap calorimeters cover $1.5 < |\eta| < 3.2$. Additionally, forward calorimeters cover $3.1 < |\eta| < 4.9$.

The barrel EM calorimeter is located in a barrel cryostat, along with the solenoidal magnet. The hadronic barrel calorimeter consists of the central barrel and two extended barrels at the each end. In Figure 2.6, it is indicated as tile barrel and tile extended barrel. The forward calorimeter is a copper and tungsten matrix with rod-shaped electrodes.

The purposes of the calorimetry in the ATLAS detector are to identify and measure the energy of the particles and jets with the sampling calorimeter type. From summing all particles transverse energy ΣE_T, the calorimetry can also measure missing transverse energy. The ATLAS calorimetry is shown in Figure 2.6.

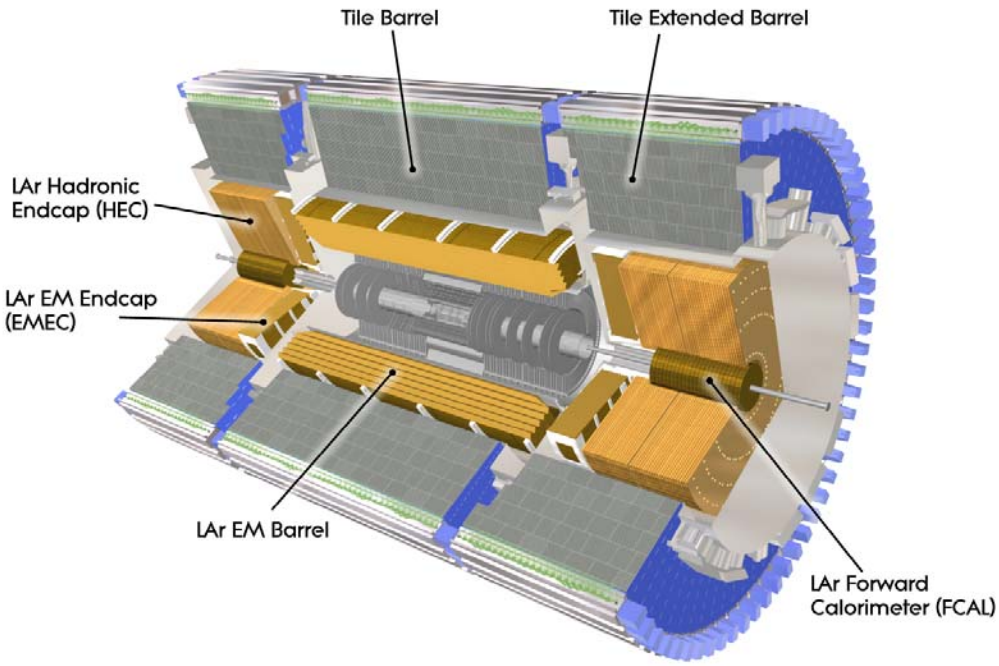

Figure 2.6: A view of the ATLAS calorimeter system.

The incoming particles are expected to be completely absorbed in the absorbers of the sampling calorimeter, in which showers are developed. The energy of a shower is measured by the active sampling layers which are interleaved with the absorbers. ATLAS uses liquid argon (LAr) and scintillating plastic for the active materials. The ATLAS team has chosen this technique because the sampling calorimeters use dense absorber planes and fine segmentation in order to identify particles and reconstruct spatial information from the calorimetry.

2.4.1 Electromagnetic calorimeter

The electromagnetic (EM) calorimeter is designed to identify electrons and photons and reconstruct them over a wide energy range. The EM calorimeter

consists of 1024 lead absorbers in inert liquid argon as an active material in an '*accordion*' shape, both for the barrel and for the end-caps. It is shown in Figure 2.7. This accordion geometry offers fast readout and good hermeticity in the EM calorimeter, and it also gives complete ϕ symmetry without cracks. Between two absorber plates, there are two liquid argon gaps of 2×1.94 mm separated by multilayer boards of readout electrodes, made of copper-clad and Kapton (300 μm thick). The total thickness of the EM calorimeter is > 24

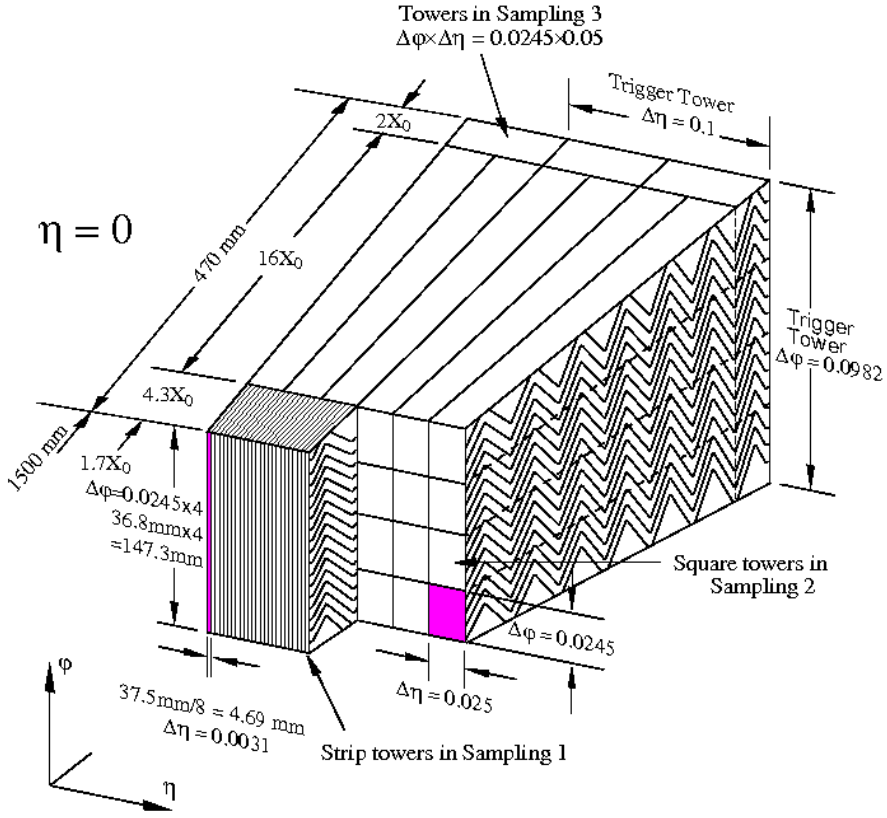

Figure 2.7: A electromagnetic calorimeter module of ATLAS.

radiation lengths (X_0) in the barrel and > 26 X_0 in the end-caps. Hence, there are three longitudinal compartments (or samplings) in the EM calorimeter. These samplings can provide a jet rejection of ~ 2000 with the hadronic calorimeter. However, the finely segmented strips ($\Delta\eta \times \Delta\phi \simeq 0.0031 \times 0.1$) in the first sampling reduces jet fragmentation from single high-p_T π^0 to identify

the two photons from the π^0 decay and low-p_T electrons produced by π. In the middle of sampling two is where electrons and photons lose most of their energy, and sampling three is to complete the shower shape and the energy measurement [30].

Test beam results of the EM barrel and the end-cap give a combined resolution for the electromagnetic calorimeter of

$$\frac{\sigma_E}{E} = \frac{10\%}{\sqrt{E}} \oplus \frac{0.4}{E} \oplus 0.7\% \ , \tag{2.3}$$

where E is in units of GeV. The first term is the statistical error due to the total number of particles in the showers, and the second term is the electronics noise, and the third term is the systematic error.

2.4.2 Hadronic calorimeter

The major purposes of the hadronic calorimeters are to identify jets including τ-jets, which are formed by the hadronization of quarks and gluons and measure their energy. In addition the hadronic calorimeter must be able to measure the total missing transverse energy from measured jet energy. The definition of the jet energy is the energy which is deposited in a cone of opening angle $\Delta R = \sqrt{\Delta\eta^2 + \Delta\phi^2}$ around the jet axis.

The hadronic calorimeter in the barrel region, the so-called *Tile Barrel* is shown in the Figure 2.6, and there is also a *Tile Extended Barrel* at each end. The barrel tile calorimeter region covers pseudorapidity $|\eta| < 1.0$, and the two extened barrel regions cover $0.8 < |\eta| < 1.7$. The sampling materials for the hadronic calorimeter are steel (absorber) and scintillating tiles (active materials), which are doped with fluorescent dye molecules. Light from excited fluorescent molecules will be detected by photomuliplier tubes (Hamamatsu R7877, PMTs) in the tile calorimeter. The scintillator tiles are arranged perpendicular to the beam axis, and wavelength-shifting fiber readouts are combined with the edges of the tiles. The grouped fibers are housed at the edge of each module. The absorbers and scintillator tile are staggered

in planes to measure the energy and location of jets in the spatial dimension. The schematic layout of a tile module is shown in Figure 2.8.

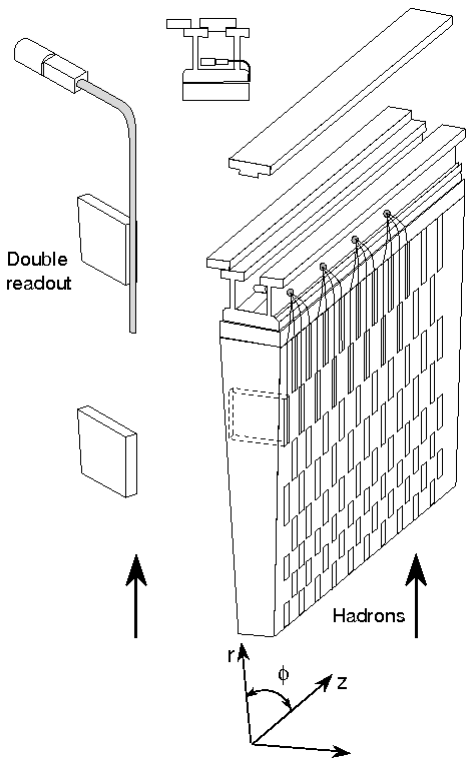

Figure 2.8: A tile module of the hadronic calorimeter of ATLAS. The various components of the readout are indicated.

The energy resolution of the hadronic calorimeter in the central barrel region is

$$\frac{\sigma_E}{E} = \frac{50\%}{\sqrt{E}} \oplus 3\% \ , \tag{2.4}$$

where E is in units of GeV and the segmentation is $\Delta\eta \times \Delta\phi = 0.1 \times 0.1$. The energy resolution in the end-cap region is

$$\frac{\sigma_E}{E} = \frac{100\%}{\sqrt{E}} \oplus 10\% \tag{2.5}$$

and it is segmentated in $\Delta\eta \times \Delta\phi = 0.2 \times 0.2$ for jet energy reconstruction [33].

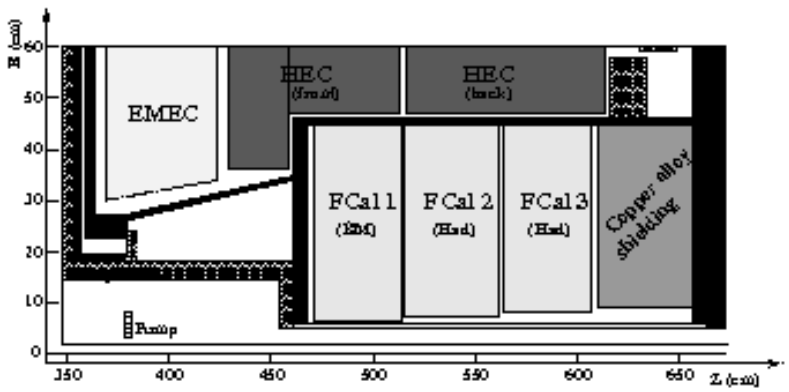

Figure 2.9: The structure of the forward calorimeter in ATLAS detector.

2.4.3 Forward calorimetry

The Forward Calorimeters (FCals) are located about 4.5 m from the interaction point. FCal is a copper-tungsten calorimeter with small liquid argon gaps. The small liquid argon gaps are mandated to avoid ion buildup problems and to lead to a faster signal.

The FCals are divided into three modules, that is, one electromagnetic module (FCal1) and two hadronic modules (FCal2 and FCal3) as shown in the Figure 2.9. The FCal1 is to remove heat and to optimize resolution. It is made of copper, while the hadronic FCal2 and FCal3 are made of tungsten to contain and minimize the lateral spread of hadronic showers.

2.5 Muon spectrometer

The muon spectrometer of the ATLAS detector is designed to reconstruct tracks passing throught the calorimeters and to trigger on muons in the central and forward region up to $|\eta| < 2.7$. There are three cylindrical layers around the z-axis of the detector in the barrel region, and muon chambers are arranged at the two end-cap regions in large circular disks. The magnetic system in the muon spectrometer is independent of the inner detector. There are eight

superconducting coils (SC) in the barrel region which are interleaved with muon chambers, and two toroidal magnets with eight coils in the end-cap region.

The muon spectrometer consists of four different types of detectors for the precision momentum measurement. They are the Monitored Drift Tube (MDT) chambers, Cathode Strip Chambers (CSCs), Resistive Plate Chambers (RPCs), and Thin Gap Chambers (TGCs). They are indicated in the Figure 2.10.

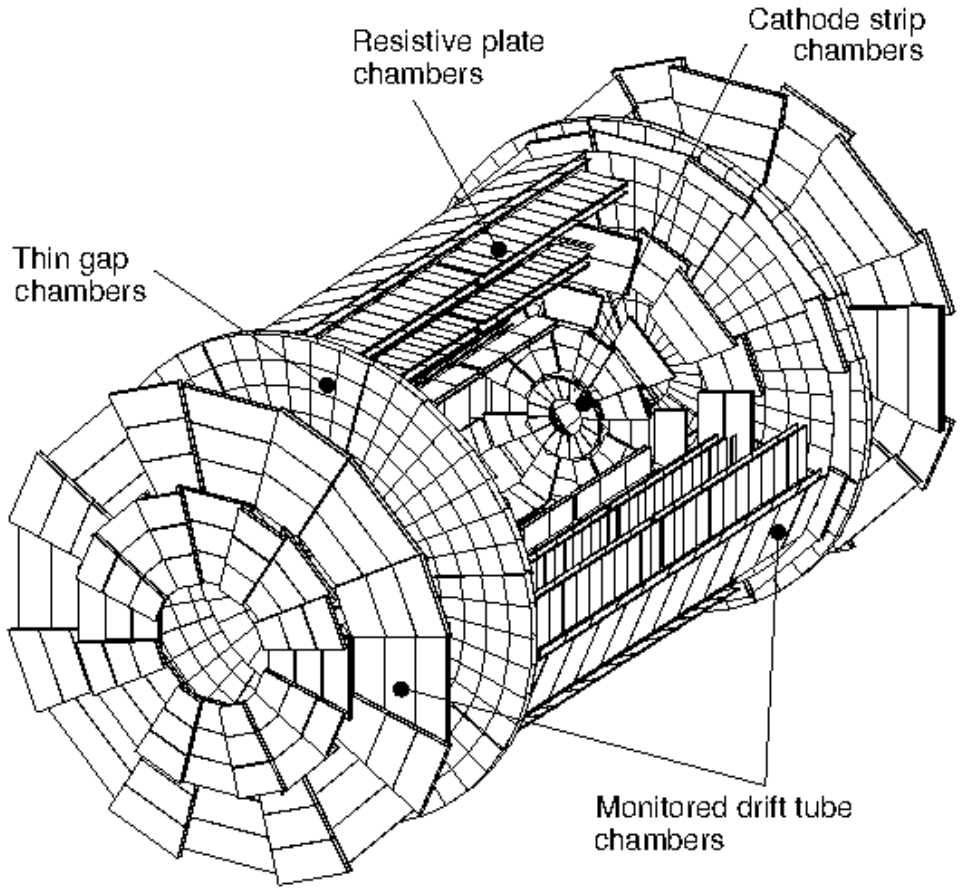

Figure 2.10: The structure of the muon spectrometer in the ATLAS detector. The four subsystems of the muon spectrometer are shown.

The Monitored Draft Tube (MDT) chamber is to measure precise muon momentum and to track muons in the muon spectrometer. It is operated at

an absolute pressure of 3 atm, which provides better measuring accuracy by a factor of $\sqrt{3}$ compared to normal pressure. There are 1172 MDT chambers in the detector over the region $|\eta| < 2$. The tubes are filled with an Ar/CO_2 gas (93:7) mixture with a central tungsten-rhenium wire with a diameter of 50 μm, at a potential of about 3080 V. When a muon passes through the MDT chamber, it will produce ions in the gas tube. These ions will drift to the central wire. The drift time to the central wire will provide the distance between a muon and the central wire. The maximum drift time from the wall to the central wire is $\sim$ 750 ns.

The Cathode Strip Chambers (CSC) are in the very forward region ($2 < |\eta| < 2.7$) as the first layer of the muon system. Thus, they require higher rate capability and good time resolution. The CSCs are designed to track muons in the bending plane (η) and in the coordinate along the tube to resolve ambiguities if there is more than one track. The resolution in the bending plane will be 60 μm and $\sim$ 5 mm in the non-bending coordinate. The time resolution is about 4 ns.

Triggering on muon tracks is one important design criterion of the muon spectrometer, and the RPCs and TGCs are designed to deliver signals inside 15-20 ns. The RPCs are arranged in the barrel region, and the TGCs are located in the end-cap region. The RPCs do not have wires, but they are gaseous parallel-plate detectors. Two resistive plastic laminate plates are separate at a distance of 2 mm by insulating spacers. A 4.9 kV/mm electric field is applied between the two plates. The space between two plates is filled with gas mixture of $C_2H_2F_4/Iso-C_4H_{10}/SF_6$. The signal will be read out by the metallic strips. Two strips are two orthogonal pick-up strips in order to measure a muon track in each projection η and ϕ. The TGCs are multi-wire proportional chambers with gas mixture of CO_2 and $n-C_5H_{12}$ in the end-cap region. The wires are located at 1.4 mm from each wall, and a distance between wires is 1.8 mm. The TGCs are used for the muon trigger and the information of the MDTs azimuthal coordinate in the bending direction.

2.6 Data acquisition and trigger system

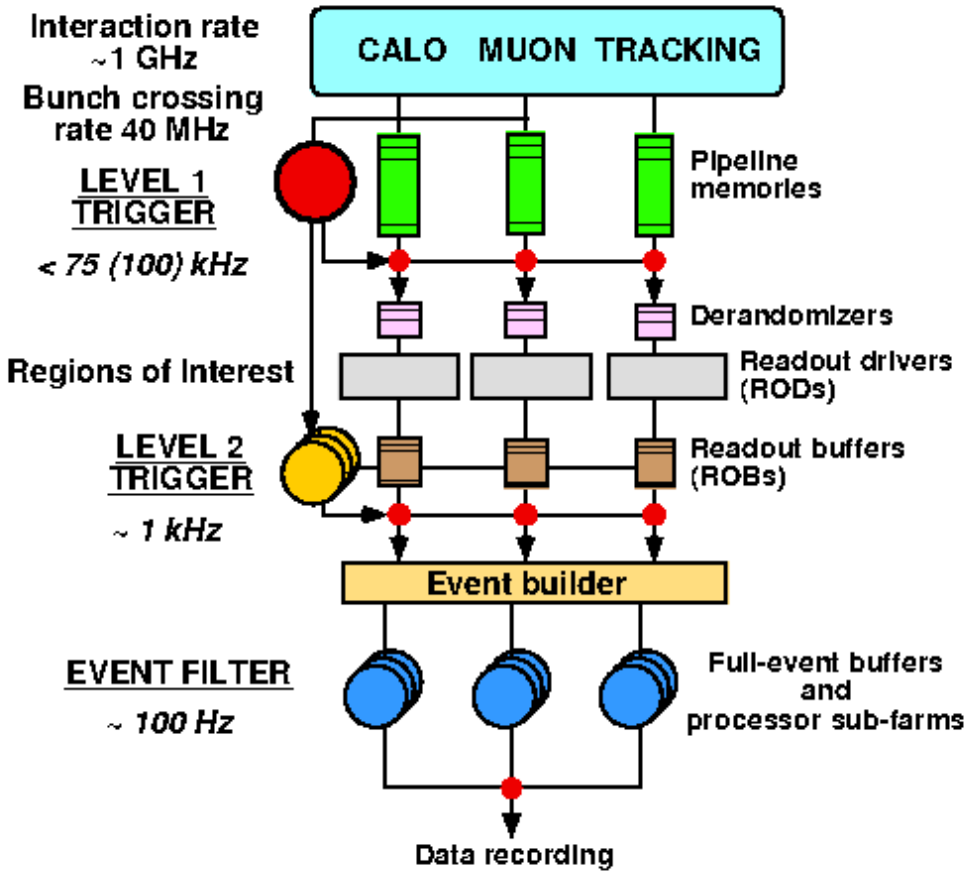

Figure 2.11: Diagram of the trigger and data acquisition system at ATLAS.

As shown in Figure 2.11, the ATLAS trigger and data acquisition (DAQ) system consists of three levels of online event selection: Level-1 (L1) trigger, Level-2 (L2) trigger, and Event Filter (EF). The L2 trigger and EF together form the High Level Trigger (HLT) [34].

The bunch-crossing rate in the LHC is 40 MHz (interaction rate $\sim 10^9$ Hz at a luminosity of 10^{34} cm^{-2}s^{-1}). However, there is too much data to store it in the limited storage space. As a result, it is necessary to reduce the rate of selected events down to $\sim$ 100 Hz through each trigger level by applying selection criteria while the rare events must retained with excellent efficiency.

The L1 trigger makes an initial selection on data from all the calorimeters and muon spectrometers. High-p_T muons are identified by the trigger chambers (the RPCs and the TGCs), and the calorimeter trigger searches for high-p_T electrons and photons, jets, and τ-leptons decaying into hadrons, as well as measures large missing transverse energy and large total transverse energy, using reduced-granularity information. The L1 trigger event rate is 75 kHz, and the L1 trigger decision time must be less than 2.5 μs. The information of accepted events by L1 trigger will be sent to the L2 trigger as Regions of Interest (RoIs) and stored in the Readout Buffers (ROBs).

The L2 trigger uses information from RoIs on the coordinates of η and ϕ and types of objects to limit the amount of data. The L1 trigger combines all the information about the different objects from sub-detectors, and then it stores them in ROBs via RoI. The L2 trigger is basically software based. If L2 trigger retrives a certain object of data from the ROBs, the RoIs produce data from the L1 trigger and gives them to the L2 trigger. The L2 trigger also includes inner detector information with the calorimeters and muon system. For electron/photon, taus, jets, and muons, L2 trigger uses dedicated algorithms to select these objects, and it also requires isolation and matching of high-p_T tracks above thresholds. The L2 trigger reduces the event rate to $\sim$ 3.5 kHz. When the L2 trigger accepts the event, it will be transfer to the EF via the DAQ system. This process of data movement is called *'Event Building'*. Before event building, an event is composed of many fragments which are in each ROB. The event builder collects a full event with many fragments from ROBs. After event building, this full event will be stored in a memory which is associated with the event filter.

The EF is the highest trigger system to reduce the event rate to $\sim$ 100 Hz, and trigger decision time is up to $\sim$ 1 s. The EF is able to access the full events with full granularity. Thus, the EF can reconstruct complete events by using offline reconstruction algorithms. The selected events from the EF are stored in mass storage farms. One can use the stored data for further study.

Chapter 3

ATLAS analysis software

Chapter 3 will describe the ATLAS software and jet finding algorithms used to carry out the data analysis. The ATLAS offline software aims to reconstruct and analyse the processed data by the ATLAS trigger and data acquisition system.

In order to find interesting signals to search for new physics in ATLAS, the ATLAS software must be able to support analysis of recorded events (real data) from the experiment as well as simulated events from a Monte Carlo event generator throughout the experiment operational lifetime. Event simulation and analysis is important to develop computer software and to tune the detector response for searches of interesting signals at ATLAS.

Thus, the ATLAS software groups provide and develop a common event processing framework, so-called *'The Athena Framework'*, which is based primarily on the C++ programming language with various supporting components and interfaces via Python scripts. The Athena framework is being used by the ATLAS collaboration as the main tool for data analysis.

In addition, jet reconstruction from the Monte Carlo generated particles will be described in this chapter in order to find the suitable jet finding algorithm for black hole events in the ATLAS detector.

3.1 ATHENA framework

The LHC experiments will produce petabytes of raw data each year. The LHC experiments will run with different operational parameters for many years, so the ATLAS experiment requires that the software must be flexible and adaptable to be maintained.

Therefore, the ATHENA framework has been developed from the GAUDI framework, which is based on realizations of component architecture, so-called Gaudi, and it is originally developed at the LHC-b experiment. The various applications and components will run in the ATHENA framework, and it will provide flexible software to analyse all event data. Now, ATHENA is a common framework for the ATLAS and LHC-b experiments. The ATHENA framework is comprised of the algorithms (the event data processing applications), system services, and data stores. The main components of the ATHENA framework are shown in Figure 3.1.

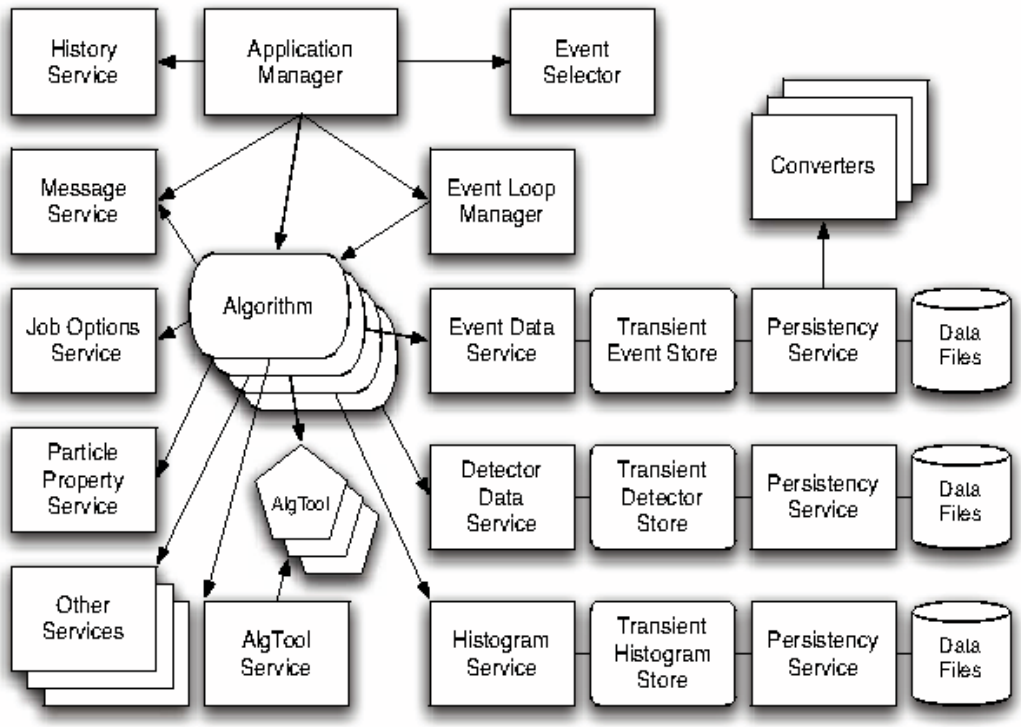

Figure 3.1: The architecture of the ATHENA framework.

The application manager knows which algorithms should be chosen and when they should response for the requests. Algorithms implement a common interface and produce some output data from input data. A top algorithm will act as the application manager and decide which algorithm produces output and when it can be used by the next algorithm. The framework ensures that the proper algorithms are executed in the right order to produce the results.

The output data from algorithms are recorded in a common place called *'Transient Data Stores (TDS)'*, so other algorithms can retrive them later. The algorithms can deposit the data objects in different transient data stores such as event data, detector data, and histograms by the characteristics of the data and their lifetime. *StoreGate* is the ATLAS transient data store.

Recored data in the TDS can be transformed to persistent form by the converters and vice versa. As a result, algorithms should access the transient data objects for further study and analysis. The converters can combine many small transient objects into a single object like a tree to minimize storage space. If it is requested to convert a persistent object into transient objects, then the converters will expand a persistent object into small transient objects.

All the services which are needed by the algorithms are for job configuration, message logging, error handling, data access, particle properties, and histogram and ntuples. As an example, the job option service (the JobOptionSvc) can be modified by users from jobOption files or from the interactive Athena prompt. It sets the Algorithm, Tools and Services. Also, the message service (the MessageSvc) can control the messages by the users via a MsgStream. Users can log specific messages such as error messages, online database or production information from certain sources via the MessageSvc. The histogram service allows users to book, fill, and analyse histograms and ntuples. On this structure of the ATHENA framework, one can generate, simulate, and digitize Monte Carlo events or analyse real data from experiments. Figure 3.2 shows the full chain of steps from generation of Monte Carlo events to production of Analysis Object Data (AOD) for further physics analysis [35] [36].

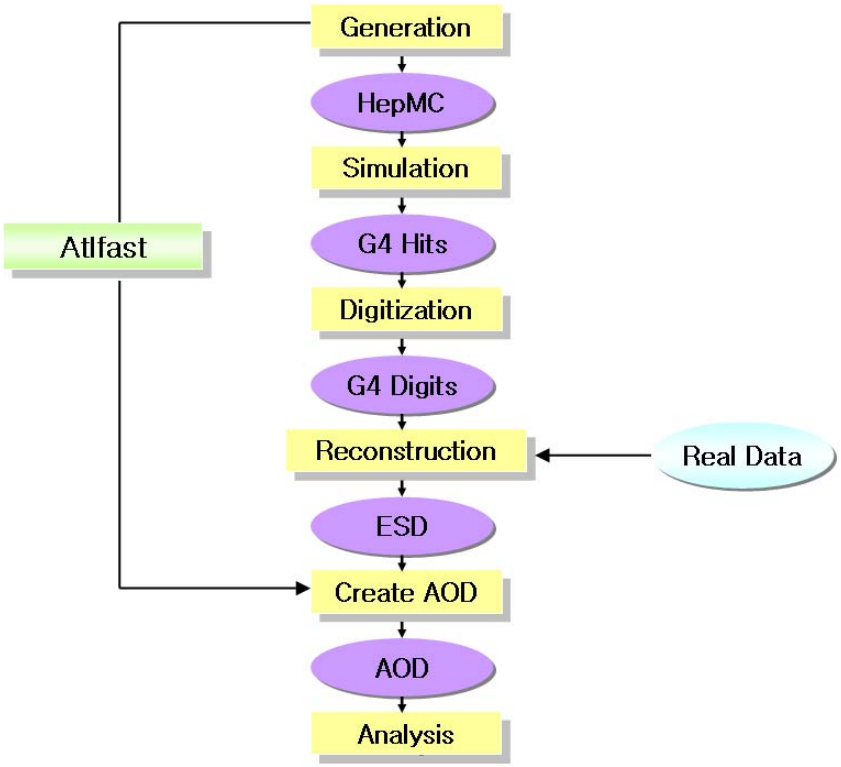

Figure 3.2: The common data-processing stages of the ATHENA framework.

Event Generation

The generation of events is the first step of the event simulation and reconstruction in the ATHENA framework. Since the LHC has not yet been operated, all of the physics analysis has been done by generated events of proton-proton collision. At present, there are several popular event generators *e.g.*, HERWIG, Pythia, Isajet, AcerMC, ComHep, AlpGen, and so on. Those generators can be run inside of ATHENA individulally. For black hole event generation, the event generator CHARYBDIS 1.0013 [37] was interfaced to the Herwig library, and then the event generator HERWIG [38] was run in ATHENA to produce the black hole events.

HepMC (High energy physics Monte Carlo)

HepMC is a object-oriented event record written in C++ for Monte Carlo event generators. Generated event data from event generation are mapped into HepMC as a common format in the StoreGate and persistent representation. Now the recorded events are for G4ATLAS simulation after a particle filtering. These data objects containing Monte Carlo truth information are read by G4ATLAS simulation based mainly on Geant4.

Simulation

In recent years, a huge amount of effort on improving the Geant4 simulation in order to provide the modeling of hadronic physics processes, and Geant4 toolkits allow physicists to build the virtual ATLAS detector with specific description of materials and to demonstrate the propagation of the particles in a framework enivornment. The G4ATLAS counts out *hits*, which have energy deposition, position, identifier, and active elements information. It has also been embodied in ATHENA for detector simulation since 2003.

Digitization

G4ATLAS simulates physics processes in the ATLAS detector, so it reads out the hits which include energy, position, and interaction information. The produced hits will response to the readout electronics and the propagation of charges or light into the media. Thus, the stage of digitization requires detail detector knowledge to build up. At the end of this step, the digitization step will produce Raw Data Objects (RDOs) which pass the event filter of the high level trigger (HLT) for reconstruction. The RDOs are similar to the real detector data. The most important role of this step is that one can compare the RDO output to real data to test the detector response for the real experiment.

Reconstruction

Reconstruction from simulated data is an important process for this thesis because the physics analysis in the next chapter has been achieved on the

reconstructed event data. Reconstruction plays the role of deriving partcle parameter and information for physical objects such as muons, electrons, photons, tau-leptons, jets, misssing transverse energy, and primary vertex.

The ESD and the AOD

The ESD contains detailed output from the reconstruction to re-run track re-fitting, jet calibration, and the first stage of particle identification. Thus, it is good for tuning of reconstruction algorithms and calibrations of the ATLAS experiment for real data. However, it does not allow to fully re-run pattern recognition from the inner detector clusters or recalibration of all the calorimeter cells because the ESD is designed to drop or compactify the largest objects. A reconstruction job will write the ESD in POOL ROOT files. It contains more information than the AOD, so the size of the ESD files are larger than the AOD ones. The sizes of data files are summarized in the Table 3.1.[5]

The AOD is produced from the ESD via the AOD builders, and it contains the necessary information to satisfy the requirements for further analysis. Various algorithms and tools are used to do it, but it contains a summary of the reconstructed event from the ESD. Thus, the size of the AOD is much smaller than the ESD files, and it is also saved as POOL ROOT files. The black hole analysis is performed on standard AOD files. The content of the AOD files will be discussed in Chapter 4. From the AOD files, one can process the addtional step for the event tags on the AOD [39].

3.2 Introduction to jet finding algorithms

Since the estimation of the black hole discovery potential requires us to apply selection criteria to jets, there will be an introduction to jets in this section. A *jet* is a stream of particles from hadronization of quarks or gluons. The proton-proton collision implies a parton-parton collision. In nature,

[5]The raw data size of 1.6 MB is estimated without pile-up. If one considers pile-up events, it will become about 3.2 MB.

Data types and items	Units	Targeted size
Raw data size	MB	1.6
ESD size	MB	0.5
AOD size	kB	100
TAG size	kB	1
Simulated data size	MB	2.0
Operation time	seconds/day	50000
	days/year	200
	days/year 2007	50
Event statistics	events/day	10^7
	events/year	2×10^9

Table 3.1: The event data sizes for different data types and related parameters for ATLAS.

quarks and gluons can not exist as a single particle as metioned in Chapter 1. As a result, the importance of measuring the total energy of jets is that it provides the inferred energy of the original quark or gluon.

In the ATLAS detector, jets are mainly detected in the calorimeter when hadronized partons interact with the detector materials. The standard jet finding algorithms in ATHENA are the seeded fixed cone4 and cone7 tower cluster with cone radius ΔR = 0.4 and 0.7 and the k_T algorithms with a distance parameter R (or D) = 1.0 in Athena release 12.0.0 version. There is only one jet algorithm implemented for jet-finding in ATHENA.

In general, one common input object (CaloCell) for jet finding algorithms is produced from the raw data or simulation stage. There are 187,652 CaloCells per event in the ATLAS calorimeter. All of CaloCell objects can not be used as input for jet finding algorithms, so a group of neighbouring CaloCells are used to build calorimeter "*towers*", and then from these towers energy "*clusters*" are constructed by CaloClusterMaker.

There are two types of energy clusters for the building blocks of jets. One

is tower clusters, and the other is topological clusters (so-called *topoclusters*). The tower cells are a fixed grid in pseudo-rapidity and azimuthal angle, and the bin size is $\Delta\eta \times \Delta\phi = 0.1 \times 0.1$. Towers can be considered as massless pseudo-particles, and cone jet finding algorithms are starting with the highest E_T tower and collect 4-momentum vector within $\Delta R = 0.4$ or $\Delta R = 0.7$. If there are no more towers within the cone radius, a new cone will start searching the next seed above 2 GeV and will locate the seed at the centre of cone. To define a jet, the cone algorithm requires at least 10 GeV as threshold energy within a certain cone radius.

On the other hand, topological clusters are seedless and have variable borders from the concept of flowing cone centres, and toplogical clusters may contain a large amount of data when they start searching futher from a stable centre. That is because the algorithm will search the entire detector. Commonly, cone algorithms pass through spliting and merging of the cones to get the final jets. However, there are several disadvantages of cone algorithms. For examples, it is hard to find the optimal configuration of cones, and it is difficult to set the standard treatment for overlapping jets within the cone size [40].

There is also a k_T clustering algorithm implemented for kinematical correlations between particles. The k_T jet finding algorithm defines jets for each pair of particles i, j with the k_T distance $d_{ij} = min(k_{ti}^2, k_{tj}^2)R_{ij}^2$, where $R_{ij}^2 = (\eta_i - \eta_j)^2 + (\phi_i - \phi_j)^2$, and k_{ti} is the transverse momentum of each particle. Then, it finds the minimum k_T distance of all particles (or recombine particles). We terminate cluster merging when the parameter D is a maximum [41].

The k_T algorithm does not have these problems, and its clustering procedure is the same both in theoretical calculations and for experimental particles. Thus, it is easy to compare the results with theory. However, it can be very slow because it adopts pre-clustering to reduce the number of kinematic objects on input. Generally, the distance parameter D has a value of 1.0 in ATHENA. Since ATLAS ATHENA release 11.0.0, the FastKt algorithms and k_T algorithms are implemented as the standard k_T algorithms, and in order to

improve the speed of processing, it does not use tower preclustering. It also requires at least 7 or 10 GeV to define the final jets. Table 3.2 shows the jet finding algorithms and the AOD content for ATLAS Release 12.0.x.

Jet finding algorithms	Parameters	AOD content
Cone4 algorithm	$\Delta R = 0.4$	Cone4TopoParticleJets
	$E_t(\text{seed}) > 2$ GeV	Cone4TowerParticleJets
	$E_t(\text{jet}) > 10$ GeV	Cone4TruthParticleJets
Cone7 algorithm	$\Delta R = 0.7$	ConeTopoParticleJets
	$E_t(\text{seed}) > 2$ GeV	ConeTowerParticleJets
	$E_t(\text{jet}) > 10$ GeV	ConeTruthParticleJets
k_T clustering	R (*or* D) $= 1.0$	k_T4TopoparticleJets
	$E_t(\text{jet}) > 10$ GeV	k_T4TowerparticleJets
		k_T6TopoparticleJets
		k_T6TowerparticleJets

Table 3.2: Summary of default jet finding algorithms in Athena 12.0.x and AOD content.

Chapter 4

Discovery potential for black holes at ATLAS

4.1 Black hole event generation at ATLAS

Several Monte Carlo event generators have been used for generating black hole events privately or officially. Among them, CHARYBDIS and CATFISH are the most refined ones as black hole event generators. (See in detail [42]) For this thesis, black hole samples are generated by CHARYBDIS version 1.0013 [37] which is interfaced, via the Les Houches accord[6] to HERWIG. The Monte Carlo event generator performs the parton shower evolution in the decay process and in the hadronization of partons. The black hole signals at the LHC are generated within the ATHENA framework with the CHARYBDIS options as follows. In Table 4.1 *'charyb'* indicates the CHARYBDIS black hole generator in the event generator jobOption files of ATHENA package. The Planck scale was 1 TeV by default.

[6]It is the standard way to input parton-level information from a matrix-elements-based generator into PYTHIA or HERWIG [43].

Description	Charybdis	Athena	values
Total dimensions (n+4)	TOTDIM	charyb 2 6	n = 2
Minimum black hole mass	MINMSS	charyb 3 5000	$M_{BH} = 5$ TeV
Maximum black hole mass	MAXMSS	charyb 4 14000	$M_{BH} = 14$ TeV
Particles in remant decay	NBODY	charyb 5 2	2 remnant
Time variation of temp.	TIMVAR	charyb 6 1	TRUE
Grey-body factors	GRYBDY	charyb 7 1	TRUE
Kinematic limit	KINCUT	charyb 8 1	TRUE

Table 4.1: The CHARYBDIS and ATHENA parameters for the generation of black hole event.

The Planck scale set to 1 TeV together with options in Table 4.1 is called the *'test case'*. In order to avoid confusion, the number of extra dimensions is always indicated in the following histograms, and the range of black hole masses is fixed to $5000 - 14000$ GeV and $8000 - 14000$ GeV.

The number of particles in the remant decay was set to 2 for the test case black hole samples. However, at the end of the Hawking evaportation of black hole decay, there is a light Planck-scale remant object, and it might decay to other particles. This phenomenon can only be understood by a quantum theory of gravity. However, this remant object can decay into several quanta and can be set in the range of 2 to 5 bodies in CHARYBDIS.

The time variation of temperature is related to the speed of black hole decay, and it was one of the parameters of black hole event generation. Grey-body factors were turned on, and they depend on the number of dimensions [44]. When the option for the kinematic limit is chosen, the generator throws away unphysical events and goes to the remnant stage. If the kinematic limit is not chosen, it throws away any unphysical events and then tries again to generate the next event.

4.2 Black hole and background samples

In order to study the characteristics of black hole events, we needed to generate black hole samples with variations in the black hole masses and in the number of extra dimensions. Therefore, three more black hole samples were generated as shown in Table 4.2.

Dataset No.	n	M_{BH} (TeV)	Cross Section (σ [pb])
5640	2	5-14	40.25
5641	2	8-14	0.34
6640	4	5-14	24.25
6641	7	5-14	22.19

Table 4.2: Monte Carlo datasets and their respective cross sections for the black hole events used in the analysis.

The Planck scale remained at 1 TeV, and the number of particles from the remant decay is 2 for all data sets. The datasets are classified by the Monte Carlo (MC) production managers of CSC (Computering System Commisioning) at ATLAS. Most of simulated or reconstructed data files dedicated for physics studies is done by the MC production managers, and they are called the CSC data sets or official data sets. However, there were time constraints and some other difficulties, so the data set 5640 was generated with ATLAS release (ATHENA) 11.3.0 and fully simulated with the ATHENA 12.0.5 but reconstructed priviately with Athena 12.0.6 version. The rest of the samples are all generated, simulated, and reconstructed privately with the same options as the officially requested data sets with Athena 12.0.x versions. The calculated cross sections are provided by Dr. Douglas Gingrich, and they can also be calculated by the event generator.

The processes top quark ($t\bar{t}$) hadronic production, $pp \rightarrow ZX,\ Z \rightarrow \tau\tau$, and $pp \rightarrow WX,\ W \rightarrow \tau\nu$ are chosen for the background samples. Of these 3 processes, due to the large cross-section, the $t\bar{t}$ process is estimated to be the

largest background for black hole events at the LHC. MCNLO was used for the matrix element calculation and the parton shower evolution. Parton decay and hadronization are done with the HERWIG event generator. The processes $pp \to ZX,\ Z \to \tau\tau$ and $pp \to WX, W \to \tau\nu$ are not major backgrounds with very small cross sections compared to the black hole signal. However, it is worth comparing the results since the particle physics team of the University of Alberta has been studying τ events. In short, these samples are all CSC data sets and reconstructed to AOD files with Athena 12.0.6 in the following table. The calculated cross sections are provided by the CSC team.

Dataset No.	Process	Cross Section (σ [pb])
5204	Hadronic decay of top quark	369
5188	$pp \to ZX,\ Z \to \tau\tau$	1640
5107	$pp \to WX,\ W \to \tau\nu$	17313

Table 4.3: Monte Carlo datasets and their respective cross sections for the backgrounds used in the analysis.

Although we did not include all SM backgrounds for this thesis, QCD dijet, $W \to e\nu$, $W \to \mu\nu$ and $W \to jjjj$ productions are the predominant backgrounds to the black hole signals. The QCD dijet background is important due to its large cross section of about 1.28×10^4 pb for $\hat{p}_T$ in the range from 280 to 2240 GeV. However, they have a lower jet p_T distribution, so the QCD dijet background is eliminated by the selection cuts. Thus, one is left with $W \to e\nu$, $W \to \mu\nu$ and $W \to jjjj$ backgrounds which have a relatively small total cross section of about 3.84 pb compared to those of the black hole signals with M_{BH} between 5 and 14 TeV.

4.3 Event selection

All ATLAS events have to be selected by the trigger system before offline study. There are 3 levels in trigger system as mentioned in Chapter 2. The

efficiencies for black hole events for various trigger conditions for each trigger level are listed in tables 4.4, 4.5, and 4.6 for 3 different CHARYBDIS samples [27]. As one can see the efficiencies for 1 jet triggers are $\gtrsim 0.99$ at all 3 levels since there are typically several high p_T jets in a black hole event. Hence, the probability of storing a black hole event for future offline study is expected to be high at ATLAS.

Trigger	LVL1	LVL2	EF
Jet100	1	1	1
Jet400	0.997	0.997	0.997
3Jet100	0.998	0.998	0.998
3Jet250	0.972	0.971	0.971
4Jet100	0.985	0.985	0.985
4Jet250	0.865	0.862	0.862

Table 4.4: Simulated jet trigger efficiencies for black hole sample 5640.

Trigger	LVL1	LVL2	EF
Jet100	1	1	1
Jet400	0.997	0.997	0.997
3Jet100	0.952	0.952	0.952
3Jet250	0.886	0.885	0.885
4Jet100	0.807	0.806	0.806
4Jet250	0.612	0.607	0.607

Table 4.5: Simulated jet trigger efficiencies for black hole sample 6640.

Trigger	LVL1	LVL2	EF
Jet100	1	1	1
Jet400	0.990	0.987	0.985
3Jet100	0.807	0.806	0.805
3Jet250	0.710	0.704	0.704
4Jet100	0.525	0.522	0.522
4Jet250	0.343	0.341	0.341

Table 4.6: Simulated jet trigger efficiencies for black hole sample 6641.

If black holes can be produced under the large extra dimension model, they will decay through Hawking radiation into all kinds of SM particles. Thus, identifying and reconstructing particles need considerable steps since

some objects can be identified as different particles. For example, a hadronically decaying tau can be identified as a photon, a tau, or a jet. Thus, the tau container in the analysis data could possibly contain jets as taus and vis versa. In addition energetic electrons, muons, and photons can also be reconstructed as jets if they have high transverse energy from the collisions. Consequently, we need to use the information of particle identification (PID) from the detector to solve this problem, and the following selections are applied on the AOD files for identification of muons, electrons, photons, taus, and jets in this order. ΔR-matching < 0.1 is applied for each particle. These selection criteria are called *Isolation cuts*.

Muon (μ)
MuidMuon collection and combined muon
$\lvert\eta\rvert < 2.5$, $p_T > 15$ GeV
Track match $\chi^2 < 20$
Track fit $\chi^2/ndf < 5$, where ndf is the number of degree freedom
$E_T cone20 < 0.2 p_T + 20$ GeV

Table 4.7: Muon isolation cuts.

The inner detector and muon spectrometer are two high precision tracking systems in the ATLAS detector. Between the two systems, there is a thick calorimeter to absorb the energy of particles to ensure the identification of muons. In order to match the tracks of muons from the inner detector to the muon spectrometer, the MuonIdentification (Muid) muon software package has been used. The Muid standalone algorithm tracks muons in the muon spectrometer, and the iPatRec package will do the track fit and track reconstruction in the inner detector. After this, *the Muid Combined algorithm* will collect information from the iPatRec and the Muid muon in order to identify muons.

Thus, the first step of the MuidMuon procedure is to connect tracks from the Muon spectrometer with the inner detector track and calorimeter infor-

mation in order to identify muons, and then *the Muid Combined algorithm* searches for tracks, which are matched by a χ^2 with 5 degrees of freedom from the parameter differences and summed covariances. For our analysis, the track match was applied with $\chi^2 < 20$ for 5 degrees of freedom, and $|\eta| < 2.5$ in the central inner detector and muon system regions. The p_T cut is applied with 15 GeV, which is a standard requirement in ATLAS analysis. After track matching, a combined fit is executed to all matches with χ^2 above a cut. We used $\chi^2/ndf < 5$ to identify muons. $E_T cone20$ is the deposited energy in a cone radius $\Delta R = 0.2$ around the muon cluster, and the selection $E_T cone20 < 0.2p_T + 20$ GeV, is proposed by the black hole team in ATLAS.

One can also use the MuidMuon Collection in the AOD files for physics analysis and choose the MuidMoun or StacoMuon Collection in the muon jobOption file under the share directory in ATHENA packages [45].

Electron (e)	Photon (γ)
$\|\eta\| < 2.5$, $p_T > 15$ GeV	$\|\eta\| < 2.5$, $p_T > 15$ GeV
Algorithm: hard egamma electron	Algorithm: hard egamma photon
IsEM&0x3ff = 0	IsEM&0xff = 0
$E_T cone20 < 0.2p_T + 20$ GeV	$E_T cone20 < 0.2p_T + 20$ GeV

Table 4.8: Electron and photon isolation cuts.

Electron and photon reconstruction and identification data are mainly from the electromagnetic calorimeter and the inner detector tracking systems. Electrons can be misidentified as jets, taus, and muons. There are two different algorithms to reconstruct electrons. One is the regular *egamma* (hard) algorithm based on calorimeter-provided seeds, and the other is the *soft egamma* algorithm based on tracking-provided seeds. For our electron identification, we used the egamma instead of soft egamma.

In addition, there is a *'cut-based'* electron identification (isEM) method. The meaning of the isEM flag is the electron/photon candidates have to pass a series of cuts on the shower shape properties in different parts of the calorimeter

and variables combining information of the inner detector and the calorimeter. If an electron/photon candidate does not pass the cuts, then a bit mask sets on the isEM flag. Thus, if isEM == 0, then this candidate passes identification cuts based on the tracking information. This is a good electron or photon. There are several expressions of the isEM mask for different parts of the inner detector criteria for ATLAS release 12.0.6 as follows:

- (isEM&0x2) == 0 : identification based only on the hadronic leakage
- (isEM&0x4) == 0 : identification based only on the 2nd sampling of the LArEM calorimeter
- (isEM&0x8) == 0 : identification based only on the 1st sampling of the LArEM calorimeter
- (isEM&0xFF) == 0 : identification based only on the calorimeter
- (isEM&0xF00) == 0 : only track cuts
- (isEM&0x7FF) == 0 : all cuts except TRT
- (isEM) == 0 : all cuts (tight cut)
- (isEM&0x3FF) == 0 : track matching, $E/|\vec{p}|$ and TRT requirements are not imposed (medium cut)
- (isEM&0x7) == 0 : ClusterFirstSampling and none of the tracking-based requirements are imposed (loose cuts).

Thus, IsEM&0x3ff == 0 for electron identification is applied as a medium cut with tracking matching, and IsEM&0xff == 0 for photon identification selections is based only on the calorimeter for our analysis. All the above cuts are applied on each particle in the AOD files with ATLAS release 12.0.6, using tag AnalysisExamples-00-14-21-02.

Jets and taus have an overlap problem with μ, e, γ, and even among themselves. If a tau decays hardronically within a jet cone radius and its energy is above 90% of jet energy, then the jet is classfied as a tau jet. In

Tau (τ)	Jet
$\|\eta\| < 2.5$, $p_T > 20$ GeV	$\|\eta\| < 2.5$, $p_T > 20$ GeV
log-likelihood ratio > 4	Tower cluster based Cone4 algorithm
TauRec algorithm	

Table 4.9: Tau and jet isolation cuts.

addition, the number of reconstructed taus is very low compared with jets and other objects for a black hole decay study, and it is also assumed that the chances of finding taus above 300 GeV is going to be extremely low in the early data at the LHC. Thus, identification of taus independantly is going to be ignored unless it effects the reconstruction of energy, momentum, and mass resolution.

However, Table 4.9 shows the isolation cuts for taus and jets. There are two algorithms for reconstructing and identifying taus. One is Tau1p3p, and the other is TauRec. They use different methods to define tau candidates. It has been recommended that Tau1p3p is for low-p_T (20-70 GeV), and this is the track-based algorithm for tau reconstruction. On the other hand, TauRec is a calo-based algorithm to reconstruct and identify hadronic taus. This algorithm requires that tau candidates should be distinguished from jets and electrons, and the likelihood variables are built for the seed to be a hadronically decaying tau. In this thesis, the TauRec algorithm will be used for tau identification and reconstruction if it is required.

In summary, ATLAS release ATHENA 12.0.6 was used for AOD analysis. The isolation cuts are applied to each object (μ, e, γ, τ, and jet) are used. The StoreGate keys include *MuidMuonCollection* for muons, *ElectronCollection* for electrons, *PhotonCollection* for photons, *TauJetCollection* for taus, and *Cone4TowerParticleJets* for jets with physics algorithms Muid Combined muons, egamma for electron and photon, TauRec for taus, and cone4 algorithm for jets.

For jet identification and reconstruction, muon, electron, photon, tau, and jets are retrived to the preselected object containers in the analysis. Although

the Cone7 algorithm shows the better result in the background processes $W \rightarrow \tau\nu$ and $Z \rightarrow \tau\tau$, the Cone4 tower-based algorithm was chosen by the black hole team of the ATLAS collaboration because black holes decay into all kinds of the SM particles with high-p_T, and it makes the events very croweded inside of jet cone. Hence, the smaller cone size is the better for very busy events with energetic particles. The histograms in Figure 4.1 show the comparison among different jet finding algorithms in ATHENA 12.0.6.

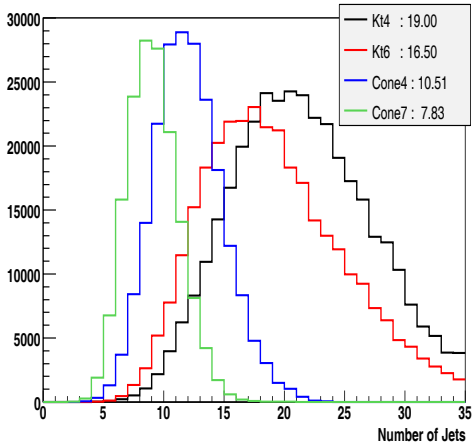

(a) Black hole 5640.

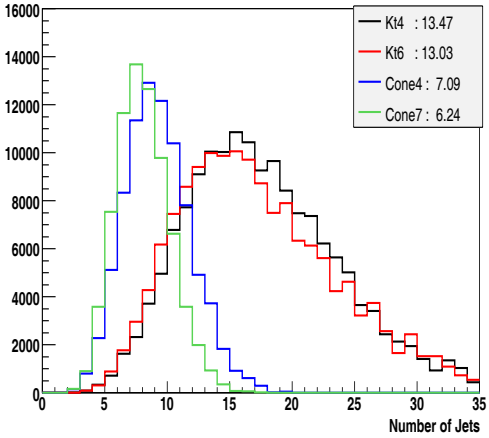

(b) Black hole 6640.

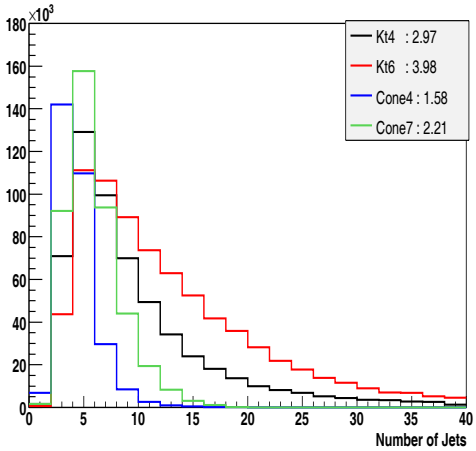

(c) $Z \rightarrow \tau\tau$.

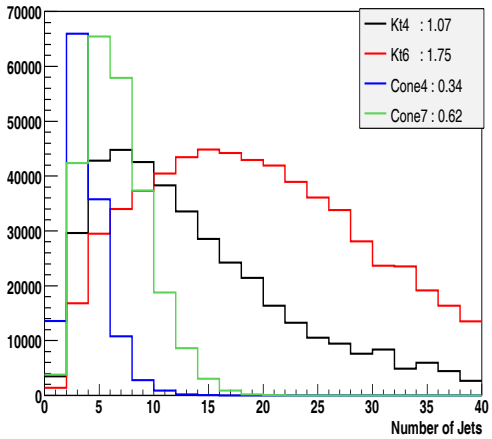

(d) $W \rightarrow \tau\nu$.

Figure 4.1: Comparison of k_T algorithms vs. cone algorithms to find a suitable jet finding algorithm for black hole events and backgrounds.

Figures 4.2 and 4.3 show p_T and η distributions of μ, e, γ, τ, and jets. The dash lines are after appling all isolation cuts with ΔR-matching > 0.1 for each object, and solid lines are without isolation cuts. Even though isolation cuts are not applied, there are still p_T and η cuts applied.

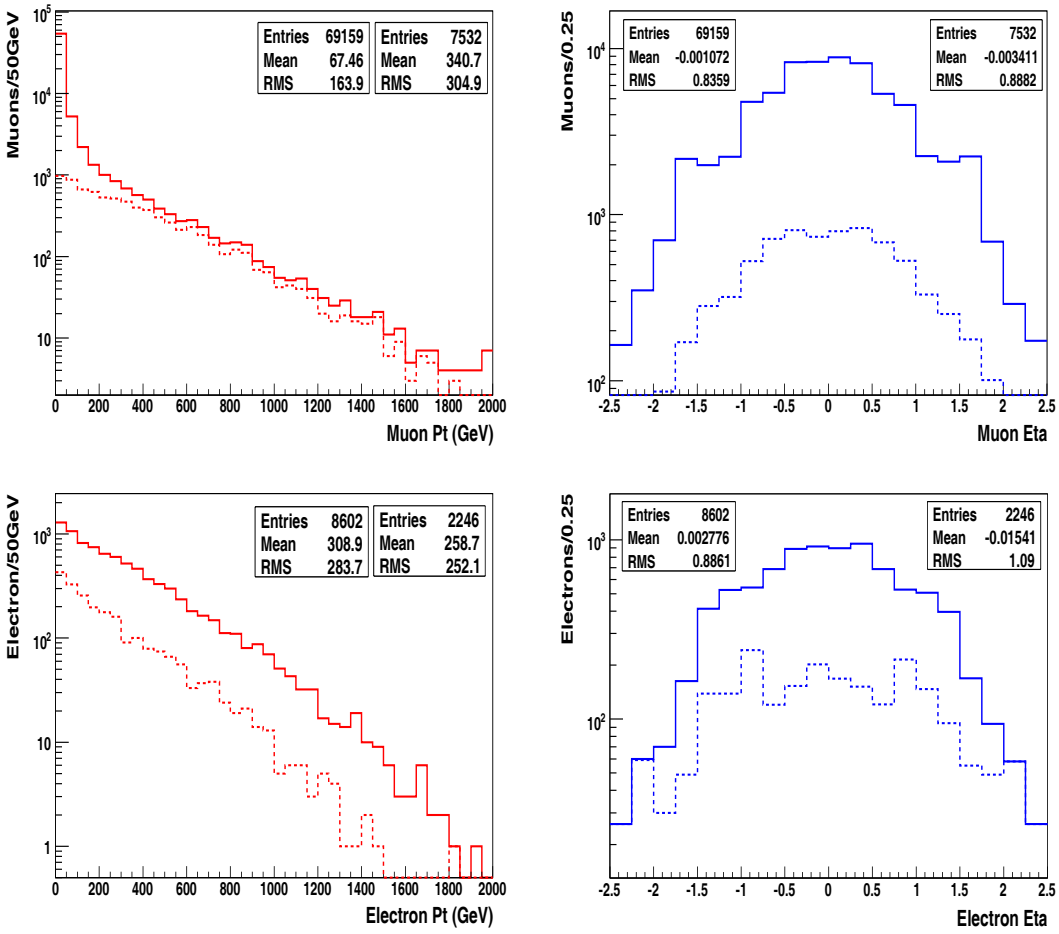

Figure 4.2: p_T and η distributions of muons and electrons before and after appling isolation cuts.

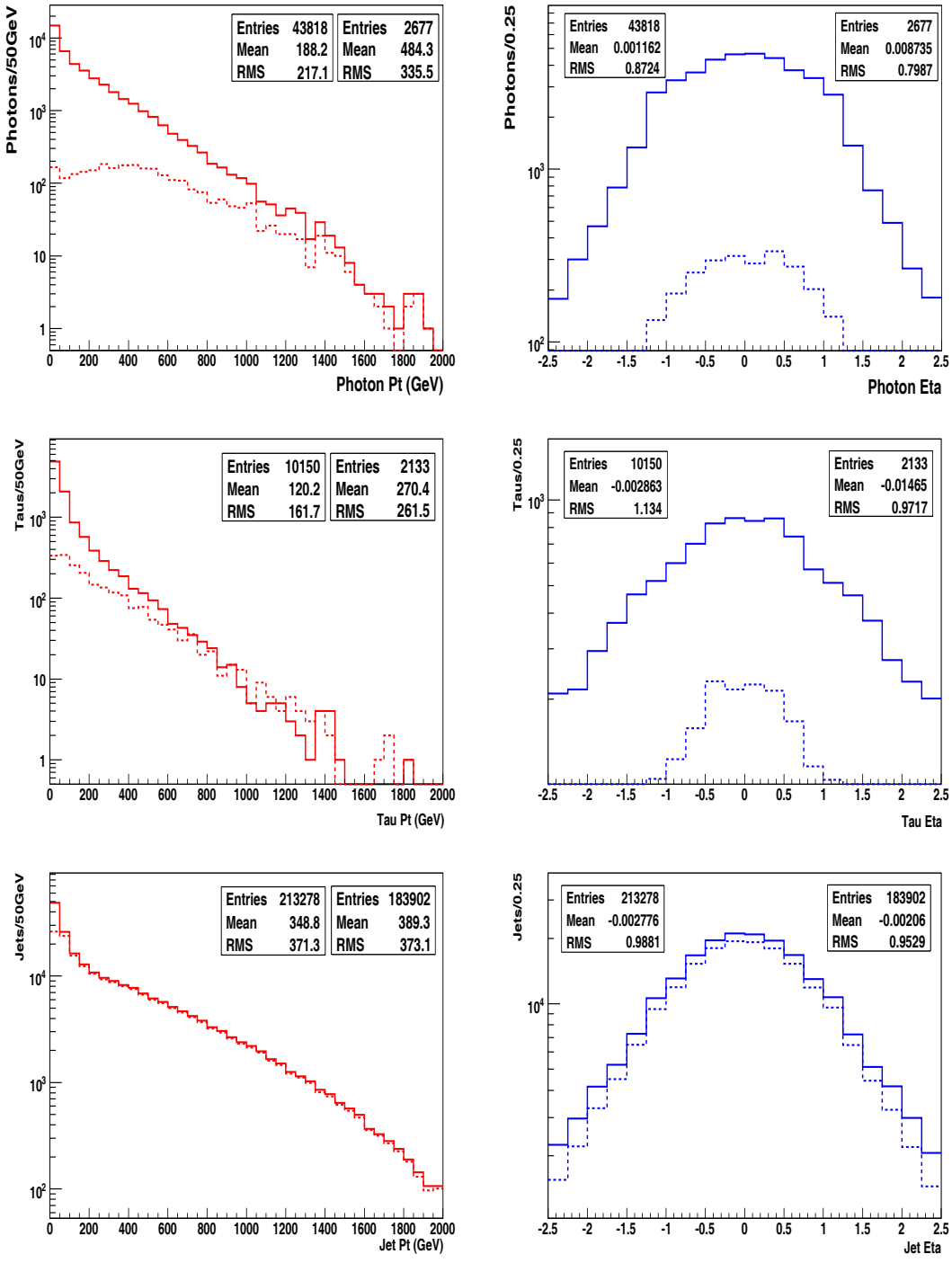

Figure 4.3: p_T and η distributions of photons, taus and jets before and after appling isolation cuts.

We also applied all the isolation cuts on the different black hole samples with different number of extra dimensions. (see Appendix A) In the jet case, there was a primary p_T cut of 20 GeV for the electromagnetic calorimeter and hadronic calorimeter. There is not such a big difference between before and after appling the cut to p_T distribution. The detector geometry tag ATLAS-CSC-01-02-00 was adopted for this study. It gives an opportunity to test the software in the different detector geometry.

Figure 4.4 shows the reconstructed missing energy (E_T) for the black hole samples. It used the refined missing E_T package in ATHENA 12.0.6. The refined missing E_T was adopted since ATHENA 12.x.x version via METRefinedAlg algorithm. Calculation of the refined calibration missing E_T starts from physics objects e/γ, μ, τ, and jets which are back-navigating to topoclusters and their Calo cells. The contribution to missing E_T from different objects is saved as $METRef\_Ele$, MET_Muon, $METRef\_Tau$, $METRef\_Jet$, and $METRef\_CellOut$ in topoclusters outside of objects. Once the algorithm finds a cell belonging to more than one object, all associations are retrived. In this way, the refined missing E_T algorithm allows to remove overlapping objects in the cells from different objects.

The missing energy is mainly produced by neutrino and graviton emission in the detector. However, Charybdis does not include the simulation of graviton emission, so the following missing energy distributions are probably underestimated. Figure 4.4 shows the missing energy distribution for the black hole events and the SM background CSC samples.

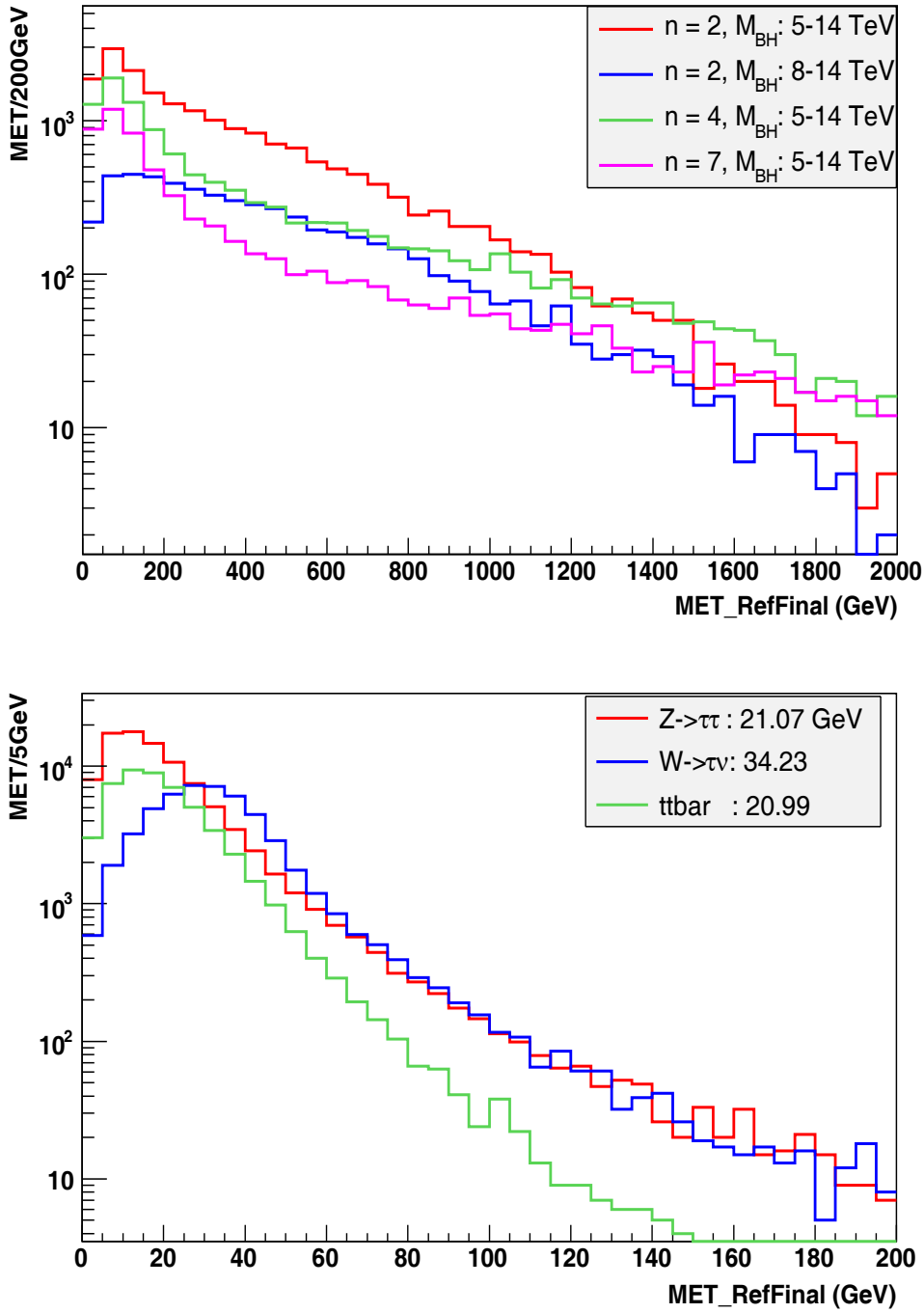

Figure 4.4: Top: Reconstructed missing energy distribution for black hole events. Bottom: Reconstructed missing energy distribution for background samples by using refined missing E_T.

4.4 The selection criteria

The following selections are applied as the standard selections for the black hole events.

- $N_{jet} \geq 4$
- $1^{st}(p_T^{jet})_{max} > 500$ GeV
- $2^{nd}(p_T^{jet})_{max} > 400$ GeV
- $3^{rd}(p_T^{jet})_{max} > 300$ GeV
- $p_T^{miss} < 100$ GeV.

Black hole events will present a large number of high-p_T final state particles because of the high mass scale and the decay process through the Hawking evaporation. Black hole masses are above 5 TeV ($M_{BH} = 5M_D$) with extra dimensions $n = 2, 4$, and 7 for the signal samples (refered to Table 4.2).

The Hawking temperature is higher in the higher extra dimensions if the black hole masses are the same value, and the effect of Hawking temperature on the black hole events is that higher temperature emits fewer particles with high energy.

Consequently, this affects the multiplicity and energy distributions in the final state, and the first event selection for discovery potential of black hole events is on the number of jets. Black hole events will have higher multiplicity than the SM background processes. This will distinguish the signal events from the SM background events. The top of Figure 4.5 shows that the number of jets decreases with increasing number of extra dimensions. The black hole mass was in the same range 5 to 14 TeV.

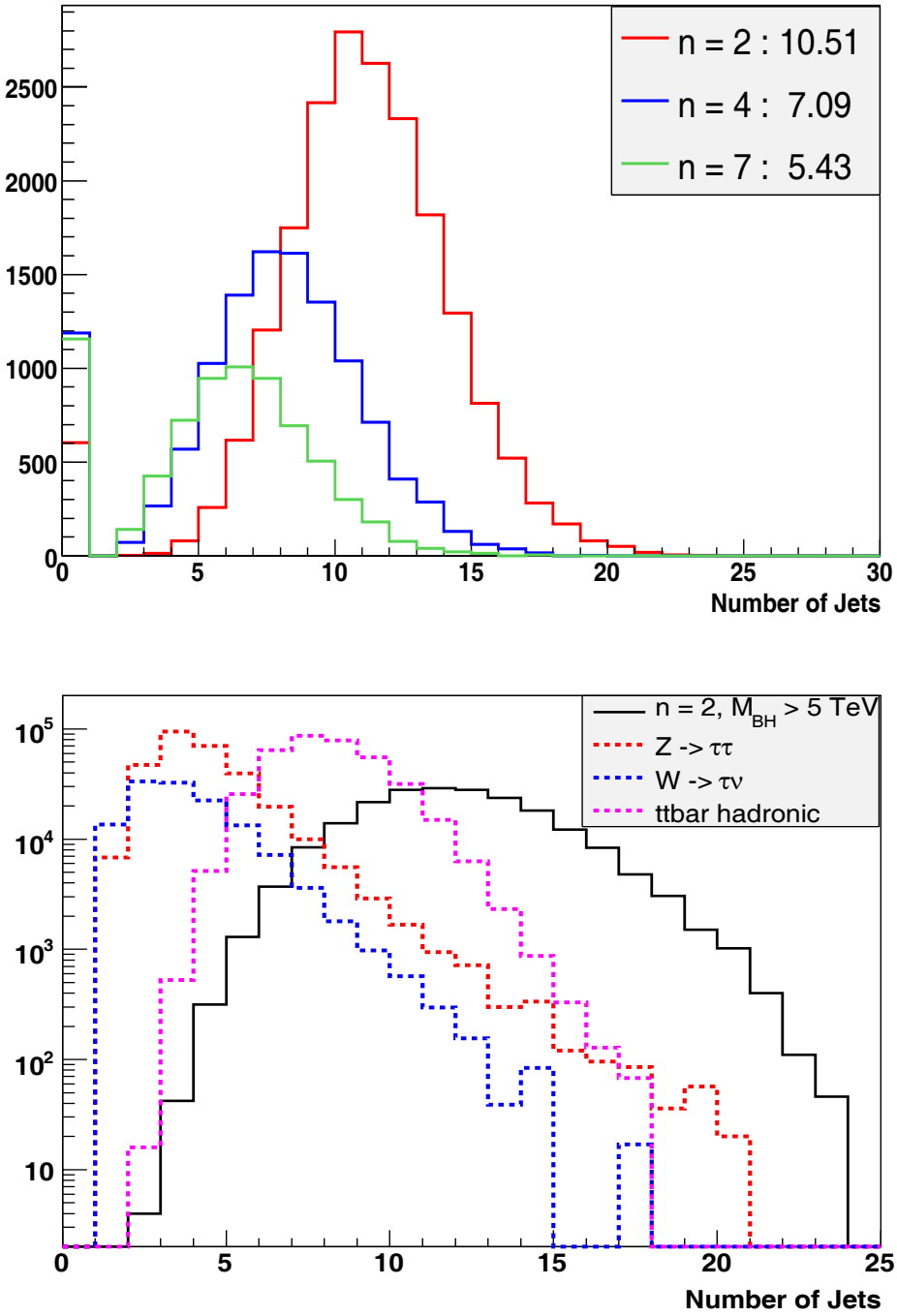

Figure 4.5: Top: The number of jets for different number of extra dimensions. Bottom: Comparison of the number of jets in black hole events (5640 sample) with the SM background samples.

The histogram in the bottom of Figure 4.5 shows the number of jets in the black hole sample 5640 with the SM background CSC samples. It shows that the first selection cut $N_{jet} \geq 4$ on jets eliminates a lot of background events. The efficiency of this selection cut will be presented in Table 4.12.

Figures 4.6 and 4.7 present the before and after applying the first selection $N_{jet} \geq 4$ on jets. For this selection, black hole sample 5640 with extra dimensions $n = 2$ and $M_{BH} = 5 - 14$ TeV is represented for black hole events in Figure 4.6 with background samples. The total number of events for signal samples and background samples are also shown in Figures 4.6 and 4.7 in order to find the efficiency for this selection cut. However, other black hole samples 5641, 6640, and 6641 are shown in Appendix B.

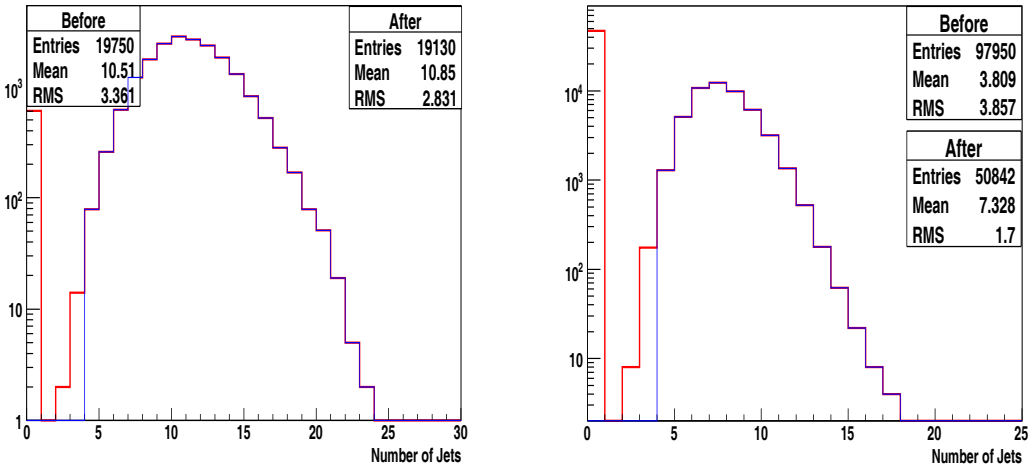

(a) Black hole 5640 (b) $t\bar{t}$

Figure 4.6: The number of jets in (a) black hole sample 5640 and (b) $t\bar{t}$ CSC sample after appling the selection cut $N_{jet} \geq 4$.

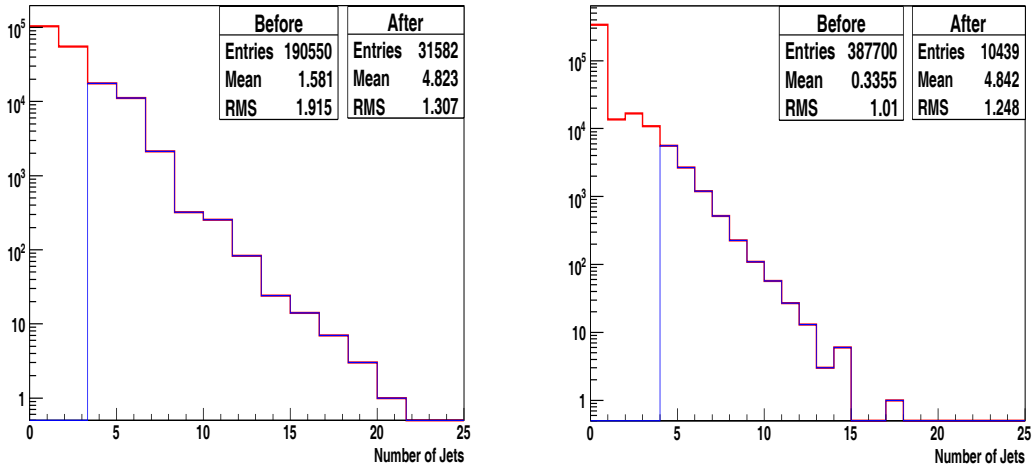

(a) $Z \rightarrow \tau\tau$ (b) $W \rightarrow \tau\nu$

Figure 4.7: The number of jets in (a) $Z \rightarrow \tau\tau$ and (b) $W \rightarrow \tau\nu$ events after appling the selection cut $N_{jet} \geq 4$.

The total number of events in all AOD files for each black hole sample is 19,750 events for black hole signal 5640 sample, 5,501 for black hole 5641 sample with the black hole mass range of $8 < M_{BH} < 14$ TeV, 11,795 events for black hole 6640 sample with extra dimension $n = 4$, and 7,183 events for black hole 6641 with extra dimension $n = 7$. In addition the total number of events in the background AOD files is 97,950 for $t\bar{t}$ events, 190,550 events for $Z \rightarrow \tau\tau$ sample, and 387,700 events for $W \rightarrow \tau\nu$ sample. These numbers are shown in Table 4.11.

After the first selection cut $N_{jet} \geq 4$, the efficiency for black holes samples are estimated to be 97%, 99%, 87%, and 76% for the 5640, 5641, 6640, and 6641 samples respectively. Thus, higher dimensional black hole lose more events after the four jet selection. It is because the black hole events with higher extra dimensions emit less particles with higher energy. On the other hand, the selection cut efficiency after the first cut for the background samples is approximately 52%, 17%, and 2.7% for $t\bar{t}$, $Z \rightarrow \tau\tau$, and $W \rightarrow \tau\nu$ respectively.

Figure 4.8 shows the p_T distribution of the first, second, third, and fourth highest p_T jets in an event. This illustrates the p_T selection cuts.

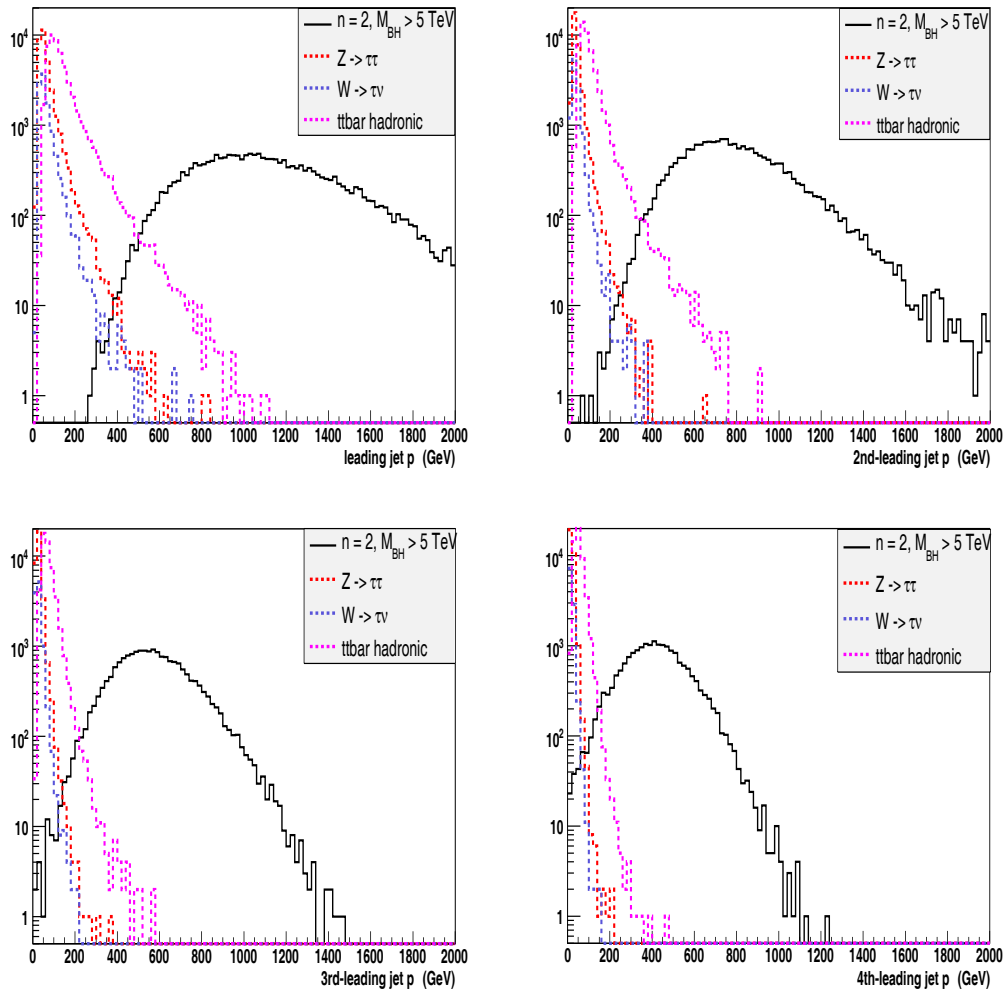

Figure 4.8: p_T distribution of first leading, 2nd leading, 3rd leading, and 4th leading jets for black hole sample 5640 and the background processes.

The requirement $p_T > 500$ GeV was applied to jets for the highest p_T in events, $p_T > 400$ GeV on the second highest p_T jets, and $p_T > 300$ GeV on the third highest p_T jets in that order. After these selection cuts, there are no events left in $W \to \tau\nu$ process, but 29 $t\bar{t}$ events, and 1 $Z \to \tau\tau$ event left. On the other hand, there are far more black hole events for each sample passing the p_T selection cuts than the background samples. The exact numbers are shown in the Table 4.8. Figures 4.9, 4.10, and 4.11 show the p_T distribution after the cuts. The histograms after the selection cuts on the black hole samples, 5641, 6640, and 6641 are shown in the Appendix B.

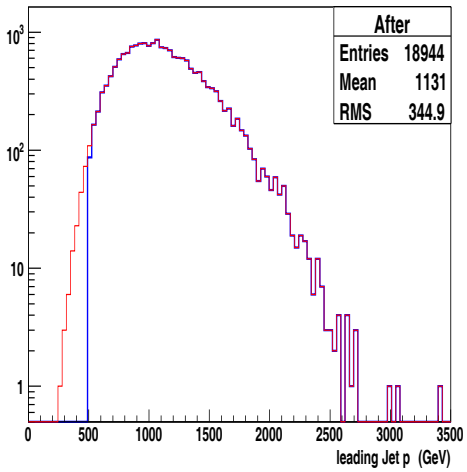

(a) Black hole 5640

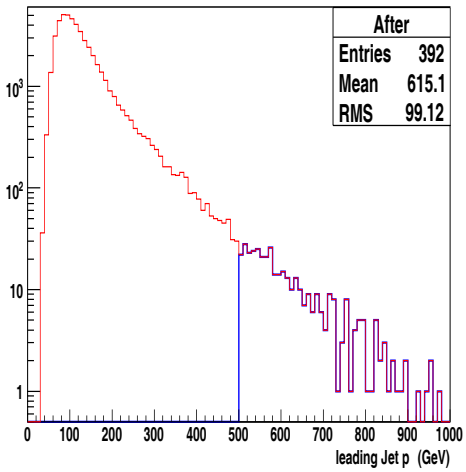

(b) $t\bar{t}$

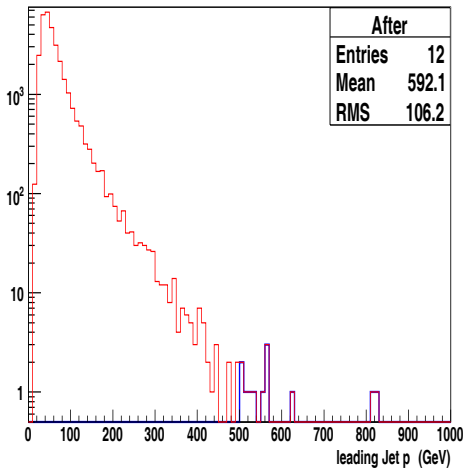

(c) $Z \rightarrow \tau\tau$

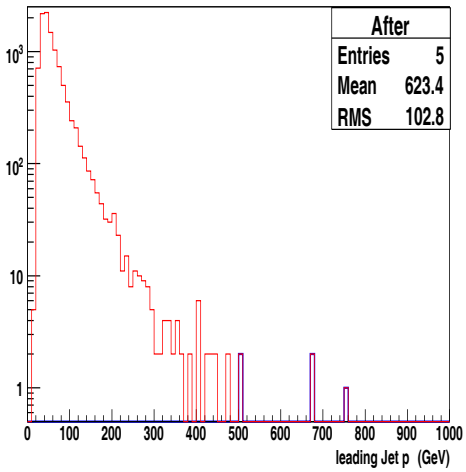

(d) $W \rightarrow \tau\nu$

Figure 4.9: p_T distributions after the selection cut, $1^{st}(p_T^{jet})_{max} > 500$ GeV.

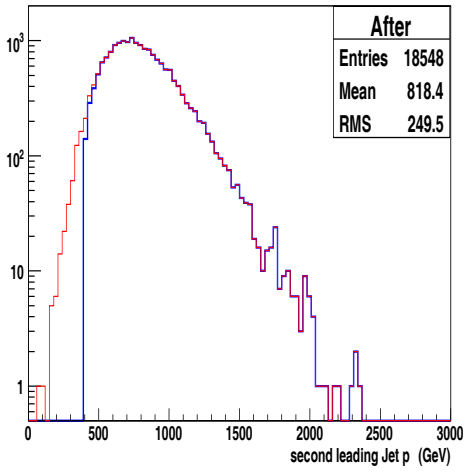

(a) Black hole 5640

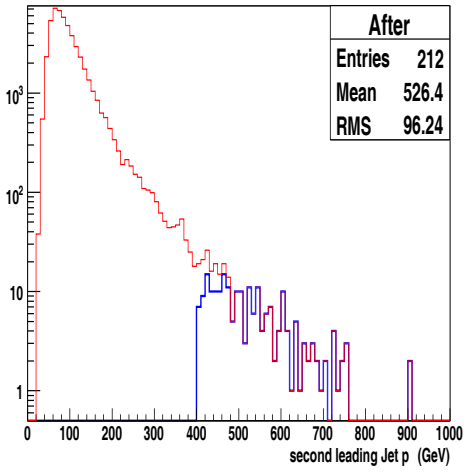

(b) $t\bar{t}$

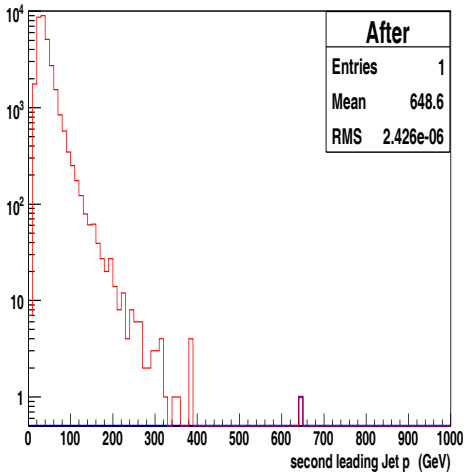

(c) $Z \rightarrow \tau\tau$

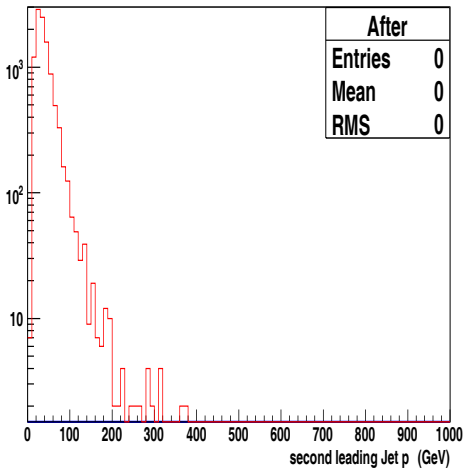

(d) $W \rightarrow \tau\nu$

Figure 4.10: p_T distributions after the selection cut, $2^{nd}(p_T^{jet})_{max} > 400$ GeV .

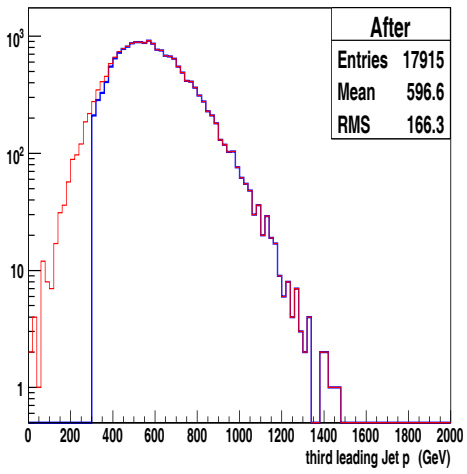

(a) Black hole 5640

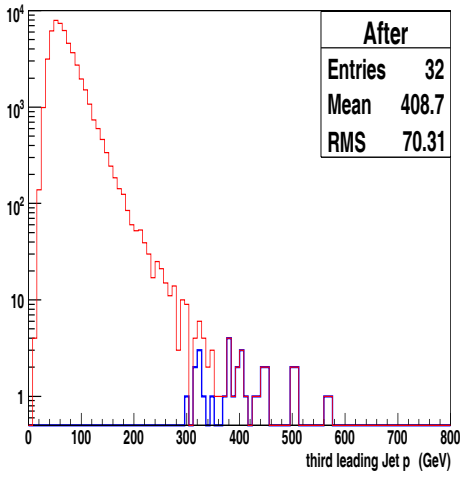

(b) $t\bar{t}$

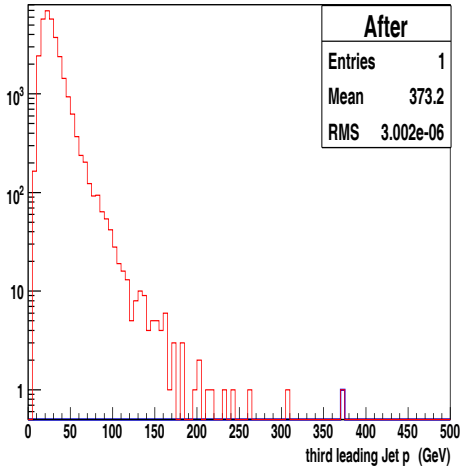

(c) $Z \rightarrow \tau\tau$

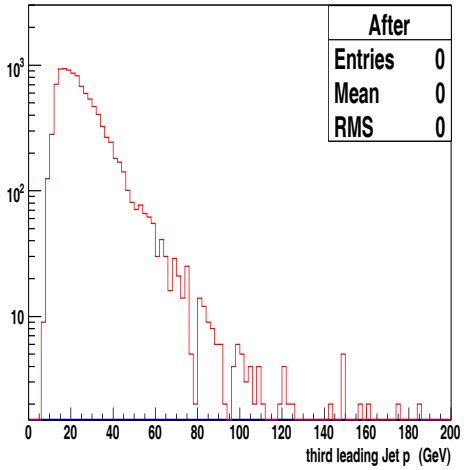

(d) $W \rightarrow \tau\nu$

Figure 4.11: p_T distributions after the selection cut, $3^{rd}(p_T^{jet})_{max} > 300$ GeV.

For the last selection cut, there is missing energy selection cut $\not{E}_T < 100$ GeV for black hole samples and $t\bar{t}$ in Figure 4.12. Thus, this selection cut rejects black hole events with high missing energy.

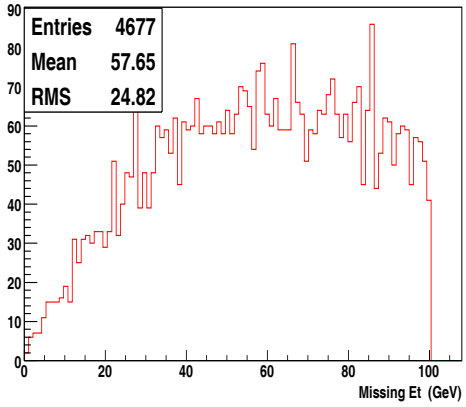

(a) Black hole 5640

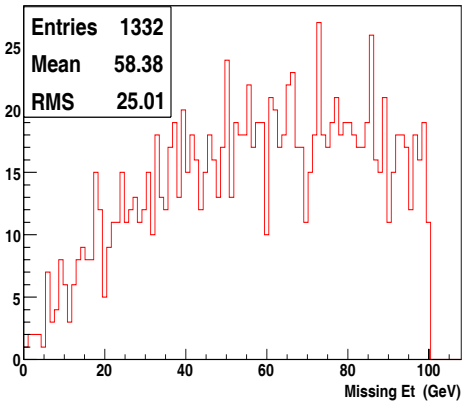

(b) Black hole 5641

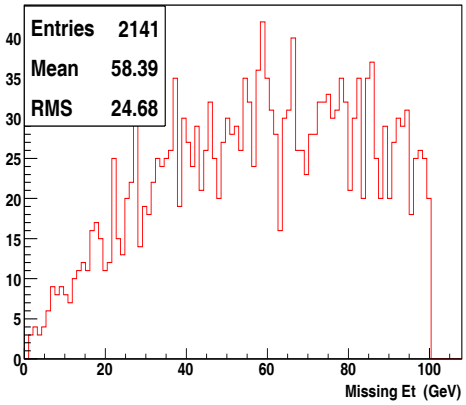

(c) Black hole 6640

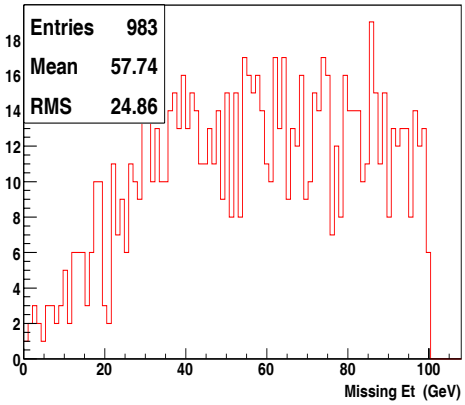

(d) Black hole 6641

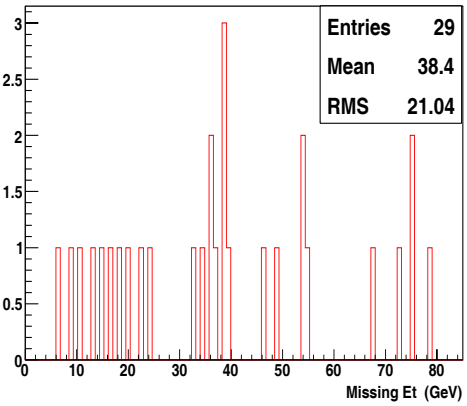

(e) $t\bar{t}$

Figure 4.12: Missing energy E_T distribution after all selection cuts.

4.5 Discovery potential for black holes

After all the selection cuts on the black hole samples and background samples, we have estimated the discovery potential for black holes in ATLAS. The black hole discovery potential for each sample has been evaluated by appling the selection criteria in section 4.4.

Table 4.7 shows the plan for luminosity at the LHC.

Parameters	Symbols	Values
Luminosity	$\mathcal{L}$	$0.5 \times 10^{33}\text{cm}^{-2}\text{s}^{-1}$ in 2007
		$2 \times 10^{33}\text{cm}^{-2}\text{s}^{-1}$ in 2008 and 2009
		$10^{34}\text{cm}^{-2}\text{s}^{-1}$ from 2010

Table 4.10: The plan for luminosity at the LHC.

The LHC will start with low luminosity and it is planning to reach the instantaneous luminosity $10^{34}\text{cm}^{-2}\text{s}^{-1}$ by 2010 as shown on the table 2.7. Therefore, the black hole discovery potential will be evaluated with time integrated luminosity $\int \mathcal{L}dt = 10$ fb^{-1} and 100 fb^{-1}. Table 4.11 shows the number of Monte Carlo events after all selection cuts, and Table 4.12 shows the cut efficiency for both signal and backgound samples.

	5640	5641	6640	6641	$t\bar{t}$	$Z \to \tau\tau$	$W \to \tau\nu$
σ (pb)	40.25	0.34	24.25	22.19	369	1640	17313
MC events	19750	5501	11795	7183	97950	190550	387700
$N_{jet} \geq 4$	19130	5463	10269	5461	50842	31582	10439
$1^{st}(p_T^{jet})_{max}$	18944	5458	10216	5436	392	12	5
$2^{nd}(p_T^{jet})_{max}$	18548	5454	9980	5274	212	1	0
$3^{rd}(p_T^{jet})_{max}$	17915	5441	8913	4115	32	1	0
p_T^{miss}	4677	1332	2141	983	29	0	0

Table 4.11: The number of Monte Carlo events which passed the event selection criteria.

	5640	5641	6640	6641
$N_{jet} \geq 4$	0.969	0.993	0.871	0.760
$1^{st}(p_T^{jet})_{max} > 500$ GeV	0.959	0.992	0.866	0.757
$2^{nd}(p_T^{jet})_{max} > 400$ GeV	0.939	0.991	0.846	0.734
$3^{rd}(p_T^{jet})_{max} > 300$ GeV	0.907	0.989	0.756	0.573
$p_T^{miss} < 100$ GeV	0.237	0.242	0.182	0.137

Table 4.12: The selection efficiency for black holes after applied the selection criteria.

	$t\bar{t}$	$Z \to \tau\tau$	$W \to \tau\nu$
$N_{jet} \geq 4$	0.519	0.166	0.0269
$1^{st}(p_T^{jet})_{max} > 500$ GeV	0.00400	6.30×10^{-5}	1.29×10^{-5}
$2^{nd}(p_T^{jet})_{max} > 400$ GeV	0.00216	5.25×10^{-6}	$< 2.58 \times 10^{-6}$
$3^{rd}(p_T^{jet})_{max} > 300$ GeV	3.27×10^{-4}	5.25×10^{-6}	$< 2.58 \times 10^{-6}$
$p_T^{miss} < 100$ GeV	2.96×10^{-4}	$< 5.25 \times 10^{-6}$	$< 2.58 \times 10^{-6}$

Table 4.13: The selection efficiency for backgrounds after applied the selection criteria.

As expected, $t\bar{t}$ processes have the highest efficiency among the background processes, but the background $W \rightarrow \tau\nu$ dominates due to its larger cross section. The first two selection cuts reject most of background events, but the black hole signal selection efficiency is above 95% in 2 extra dimensions. The selection efficiency is decreased by increasing the number of extra dimensions as shown in Table 4.12.

The number of Monte Carlo events for the black hole signal and backgrounds need to be normalized for the time integrated luminosity in order to estimate how many events can be produced in a certain period of time at ATLAS.

According to Table 4.7, $L = \int \mathcal{L}dt \simeq 15.77$ fb^{-1} for year 2007, ~ 63.07 fb^{-1} for 2008 and 2009, and ~ 315 fb^{-1} by 2010. In fact, the LHC has not yet started. When one considers the complicated environment for operating the LHC collider, the luminosity will not be the exact numbers as predicted. Thus, we will normalize the number of Monte Carlo events with the time integrated luminosity $L = \int \mathcal{L}dt = 10$ fb^{-1} which is closed to the first year luminosity at the LHC and 100 fb^{-1} which will give the same amount of data taking at the highest luminosity. The physical number of event can be estimated according to equation 4.1:

$$N = L\sigma\varepsilon_{cut}, \tag{4.1}$$

where N is the number of events observed, and ε_{cut} is the signal selection efficiency. The cross sections are shown in the Table 4.11 and time is for 1 year. The normalized number of events with the time integrated luminosity $L = \int \mathcal{L}dt = 10$ fb^{-1} for black hole events and backgrounds are shown in Tables 4.14 and 4.15 respectively.

$L = 10\text{fb}^{-1}$	5640	5641	6640	6641
σ (fb)	4.025×10^4	340	2.425×10^4	2.219×10^4
Physical events	4.025×10^5	3400	2.425×10^5	2.219×10^5
After selection cuts				
$N_{jet} \geq 4$	3.900×10^5	3376.2	2.112×10^5	1.686×10^5
$1^{st}(p_T^{jet})_{max}$	3.860×10^5	3372.8	2.100×10^5	1.680×10^5
$2^{nd}(p_T^{jet})_{max}$	3.779×10^5	3369.4	2.052×10^5	1.629×10^5
$3^{rd}(p_T^{jet})_{max}$	3.651×10^5	3362.6	1.833×10^5	1.271×10^5
p_T^{miss}	9.539×10^4	822.8	4.414×10^4	3.040×10^4

Table 4.14: The normalized number of black hole events with luminosity 10 fb^{-1}.

$L = 10\text{fb}^{-1}$	$t\bar{t}$	$Z \to \tau\tau$	$W \to \tau\nu$
σ (fb)	36.9×10^4	164×10^4	1731×10^4
Physical events	36.9×10^5	164×10^5	1731×10^5
After selection cuts			
$N_{jet} \geq 4$	1.915×10^6	2.722×10^6	4.656×10^6
$1^{st}(p_T^{jet})_{max}$	1.476×10^4	1033.2	2233
$2^{nd}(p_T^{jet})_{max}$	7970	86.1	< 446.6
$3^{rd}(p_T^{jet})_{max}$	1206	86.1	< 446.6
p_T^{miss}	1092	< 86.1	< 446.6

Table 4.15: The normalized number of background events with luminosity 10 fb^{-1}.

In the signal sample 5640, if the LHC starts operating with luminosity 10 fb^{-1} for the first year, one can see 4.0×10^5 black hole events with $n = 2$ and 5 TeV $< M_{BH} <$ 14 TeV. After applying all selection cuts, there is the possibility to observe 9.5×10^4 events in the ATLAS detector. On the other hand, before the selection cuts, the backgrounds are the dominant processes, but they are mostly rejected by the selection cuts.

However, one important fact that we need to consider is the statistical significance of the background samples according to the ratio of the background cross sections with the black hole cross sections. The $t\bar{t}$ cross section is about 9 times larger than the cross section of the black hole sample 5640, so if the $t\bar{t}$ process is to be statistically significant enough to support the results, there needs to be 9 times larger number of events compared to the black hole sample 5640. We need about 180,910 Monte Carlo events for the $t\bar{t}$ process. Thus, we need to get 82,960 more Monte Carlo events for $t\bar{t}$ background sample to compare with the black hole 5640 sample. Although the number of events for background samples are not statistically sufficient, the results can give an estimation of the discovery potential of black hole events at ATLAS.

Subsequently, we will calculate the conventional condition for a discovery of a new phenomenon at ATLAS. In order to claim discovery,

$$S/\sqrt{B} \geq 5 \quad \text{and} \quad S \geq 10. \tag{4.2}$$

Where S is the number of signal events and B is the number of background events which pass the event selection criteria. These conditions are used in the analysis of Higgs boson events at ATLAS. In order to define the sensitivity for discovery, generally the 5σ limit is used as shown above. From Table 4.8, the ratio of black hole events to $t\bar{t}$ events, and the significance of black hole samples $S/\sqrt{B}$ is calculated in Table 4.13. The backgrounds $Z \rightarrow \tau\tau$ and $W \rightarrow \tau\nu$ are rejected completely after the second leading and third leading p_T cuts.

	5640	5641	6640	6641
S/B	161.27	45.93	73.83	33.90
$S/\sqrt{B}$	868.50	247.35	397.57	182.54

Table 4.16: The signal to background ratio and black hole signal significance.

Table 4.13 shows that the significance of all the black hole samples exceeded far more than 5σ in order to claim a new signal. We conclude that if black holes are produced at the LHC, they will be very distinguishable from the SM backgrounds at ATLAS. However, in this thesis, we could not include all the background processes for the black hole signal, so careful consideration is needed to claim the discovery potential of black hole at ATLAS with such high possibility.

Chapter 5

Conclusion

In this thesis, we have estimated the discovery potential for black hole production in ATLAS. We used four black hole samples with different extra dimensions $n = 2, 4$, and 7 in the mass ranges 5 TeV $< M_{BH} <$ 14 TeV and 8 TeV $< M_{BH} <$ 14 TeV. These signal samples were generated with the Planck scale $M_P = 1$ TeV. The black hole samples are generated in ATHENA by CHARYBDIS version 1.0013 which is interfaced to Herwig. For the background samples, we used $t\bar{t}$, $Z \rightarrow \tau\tau$, and $W \rightarrow \tau\nu$ samples, which were CSC5204, CSC5188, and CSC5107 data sets. Although the backgrounds $Z \rightarrow \tau\tau$ and $W \rightarrow \tau\nu$ are expected to be rejected by the first selection cut on the number of jets, they were chosen because taus are one of subjects for the particle physics group at the University of Alberta, and also $t\bar{t}$ events are estimated to be the largest contribution to the background due to its large cross section and branching ratio at the LHC.

The black hole events will decay under Hawking evaporation to all kinds of SM particles in ATLAS. Those particles from black hole events are very energetic and are highly populated in an event. From the characteristics of the black hole events, the selection cuts are set on the number of jets, the three leading p_T jets, and missing energy. However, there are a large number of algorithms involved in particle identification and reconstruction at ATLAS,

and there is misidentification of particle objects in software. As a result, it is necessary to remove misidentified and overlapping muons, electrons, photons, taus, and jets. These were the isolation cuts in Table 4.4, 4.5, and 4.6 in Chapter 4. After appling all the isolation cuts on each particle object, we put the black hole selection cuts on the jet. The number of Monte Carlo events which passed the cuts are shown in Table 4.11, and cut efficiencies for each selection are in Table 4.12.

The cut efficiencies for the black hole samples are around 0.23 to 0.13. On the other hand, the cut efficiencies for backgrounds are less than 10^{-4}. We have applied all the section cuts to the analysis of black holes, and in this case, we can observe 9.5×10^4 events for 5640, 822.8 events for 5641, 4.4×10^4 events for 6640, and 3.04×10^4 events for 6641 with total luminosity 10 fb^{-1}. When we compared these with the SM backgrounds, the ratios S/B were approximately 161 for 5640, 45 for 5641, 73 for 6640, and 33 for 6641. These give the significance for discovering black hole events with ATLAS far larger than 5σ.

The black hole events in ATLAS are very distinguishable from the SM background processes. If black holes are produced in ATLAS, then we must see them after analysing the events. However, we did not have all SM backgrounds for this thesis, so one needs to consider that this is a partial discovery potential for black hole events in ATLAS with three background samples.

Bibliography

[1] The LEP Higgs Working Group. *Standard Model Higgs Boson at LEP: Results with the 2000 Data Request for Running in 2001.* Website, 2000. `http://lephiggs.web.cern.ch/LEPHIGGS/papers/doc_nov3_2000.ps`.

[2] SNO Collaboration. *Direct Evidence for Neutrino Flavor Transformation from Neutral-Current Interactions in the Sudbury Neutrino Observatory. Phys. Rev. Lett*, 89:011301, 2002.

[3] David Griffiths. *Introduction to Elementary Particles.* ISBN 0-471-60386-4. John Wiley & Sons, Inc., 1987.

[4] S. L. Glashow. *Partial-Symmetries of weak Interaction. Nucl. Phys.*, 22:579, 1961.

[5] S. Weinberg. *A Model of Leptons. Phys. Rev. Lett.*, 19:1264, 1967.

[6] G. Arnison et al. *Experimental observation of isolated large transverse energy electrons with associated missing energy at* $\sqrt{s}$ *= 540 GeV. Phys. Lett. B*, 122:103, 1983.

[7] UA1 Collaboration. G. Arnison et al. *Experimental observation of lepton pairs of invariant mass around 95 GeV at the CERN SPS collider. Phys. Lett. B*, 126:398, 1983.

[8] Howard Georgi and S. L. Glashow. *Unity of All Elementary-Particle Forces. Phys. Rev. Lett.*, 32:438–441, 1974.

[9] Gordon Kane. *Modern Elementary Particle Physics.* ISBN 0-201-62460-5. Perseus Books, 1993.

[10] Dimitri Bourilkov. *Gauge coupling unification, SUSY scale and Strong coupling running.* Website, 2005. `http://panic05.lanl.gov/abstracts/499/Bourilkov_499_panic05.ppt`.

[11] Milada Margarete Mühlleitner. *Higgs Particles in the Standard Model and Supersymmetric Theories. hep-ph/0008127*, page 1, 2000.

[12] Sijbrand de Jong. *Tests of the Electroweak Sector of the Standard Model. hep-ex/0512043*, page 1, 2005.

[13] Maarten C. Brak. *The Hierarchy Problem in the Standard Model and Little Higgs Theories*, 2004. `http://www.nikhef.nl/pub/theory/masters-theses/maarten_brak.pdf`.

[14] Christopher M. Harris. *Physics Beyond the Standard Model: Exotic Leptons and Black Holes at Future Colliders. hep-ph/0502005*, page 1, 2005.

[15] S. Dimopoulos N. Arkani-Hamed and G.R. Dvali. *The Hierarchy Problem and New Dimensions at a millimeter. Phys. Lett. B*, 429:263–272, 1998.

[16] S. Dimopoulos N. Arkani-Hamed and G.R. Dvali. *Phenomenology, astrophysics, and cosmology of theories with submillimeter dimensions and TeV scale quantum gravity. Phys. Rev. D*, 59:086004, 1999.

[17] L. Randall and R. Sundrum. *Large Mass Hierarchy from a Small Extra Dimension. Phys. Rev. Lett.*, 83:3370, 1999.

[18] L. Randall and R. Sundrum. *An Alternative to Compactification. Phys. Rev. Lett.*, 83:4690, 1999.

[19] Riccardo. Rattazzi Gian.F. Giudice and James.D. Wells. *Quantum Gravity and Extra Dimensions at High-Energy Colliders. Nucl. Phys. B*, 544:3, 1999.

[20] Y. Grossman N. Arkani-Hamed and M. Schmaltz. *Split fermions in extra dimensions and exponentially small cross-sections at future colliders. Phys. Rev. D*, 61:115004, 2000.

[21] R.C Myers and M.J. Perry. *A Model for High Engergy Scattering in Quantum Gravity. Ann. Phys.*, 172:304, 1986.

[22] T. Banks and W. Fischler. *A Model for High Engergy Scattering in Quantum Gravity. hep-th/9906038*, page 1, 1999.

[23] Savas Dimopoulos and Greg Landsberg. *Black Holes at the LHC. Phys. Rev. Lett.*, 87, 2001.

[24] S. W. Hawking. *Particle creation by black holes. Commun. Math. Phys.*, 43:199, 1975.

[25] H. Goldberg L. Anchordoqui, J. Feng and A. Shapere. *Black Holes from Cosmic Rays: Probes of Extra Dimensions and New Limits on TeV-Scale Gravity. Phys. Rev. D*, 65:124027, 2002.

[26] S. ASK. *search for extra dimensions at LEP. arXiv:hep-ph/0410004v1*, 2004.

[27] The ATLAS Collaboration. *Microscopic Black Hole Production at the LHC: the Discovery Reach of the ATLAS Experiment.* `http://indico.cern.ch/getFile.py/access?resId=0&materialId=4&confId=24490`.

[28] P. Lefévre and T. Pettersson. *The Large Hadron Collider:conceptual design. CERN-AC-95-05-LHC*, 1995.

[29] R. Schmidt. *Status of the LHC*, 2002. `http://epaper.kek.jp/e02/PAPERS/MOXGB003.pdf`.

[30] ATLAS Collaboration. *ATLAS Technical Proposal for a General-Purpose pp Experiment at the Large Hadron Collider at CERN. CERN/LHCC/94-43*, 1994.

[31] ATLAS Collaboration. *ATLAS Detector and Physics Performance Technical Design Report. CERN/LHCC/99-14*, 1999.

[32] ATLAS Inner Detector Collaboration. *ATLAS Inner Detector Technical Design Report. CERN/LHCC/97-16*, 1997.

[33] ATLAS Tile Calorimeter Collaboration. *Tile Calorimeter Technical Design Report. CERN/LHCC/96-42*, 1996.

[34] ATLAS Level-1 Trigger Collaboration. *Level-1 Trigger Technical Design Report. CERN/LHCC/98-14*, 1998.

[35] G. Barrand et al. *GAUDI-A software architecture and framework for building HEP data processing applications. Comp. Phys. Comm.*, 140:45–55, 2001.

[36] ATLAS Computing Group. *ATLAS Computing Technical Design Report. CERN/LHCC/2005/022*, 2005.

[37] P. Richardson C.M. Harris and B.R Webber. *CHARYBDIS:a black hole event generator. JHEP*, 08:033, 2003.

[38] G. Corcella et al. *HERWIG 6.5. arXiv:hep-ph/0011363*, 2003.

[39] Kétévi A. Assamagan et al. *Final report of the ATLAS AOD/ESD Definition Task Force. ATLAS-SOFT-2004-006*, 2004.

[40] Gerald C. Blazey et al. *Run II Jet Physics. hep-ex/0005012v2*, 2000.

[41] Matteo Cacciari and Gavin P. Salam. *Dispelling the N^3 myth for the k_t jet-finder. arXiv:hep-ph/0512210v1*, 2005.

[42] Douglas M. Gingrich. *Comparison of Black Hole Generators for the LHC. arXiv:hep-ph/0610219*, 2006.

[43] Stephen Mrenna Torörn Sjöstrand and Peter Skands. *PYTHIA 6.4 Physics and Manual. arXiv:hep-ph/0603175*, 2006.

[44] C.M. Harris and P. Kanti. *Hawking Radiation Black Hole: Exact Results for the Schwarzschild Phase. JHEP*, 0310:014, 2003.

[45] J. Shank et al. *Muon identification and combined reconstruction for the ATLAS detector at CERN-LHC.* In *Astroparticle, particle and space physics, detectors and medical physics applications.* World Scientific Publishing Co. Pte. Ltd., 2003.

Appendix A

Isolation cuts

The following histograms present before and after the isolation cuts for muons, electrons, photons, taus, and jets.

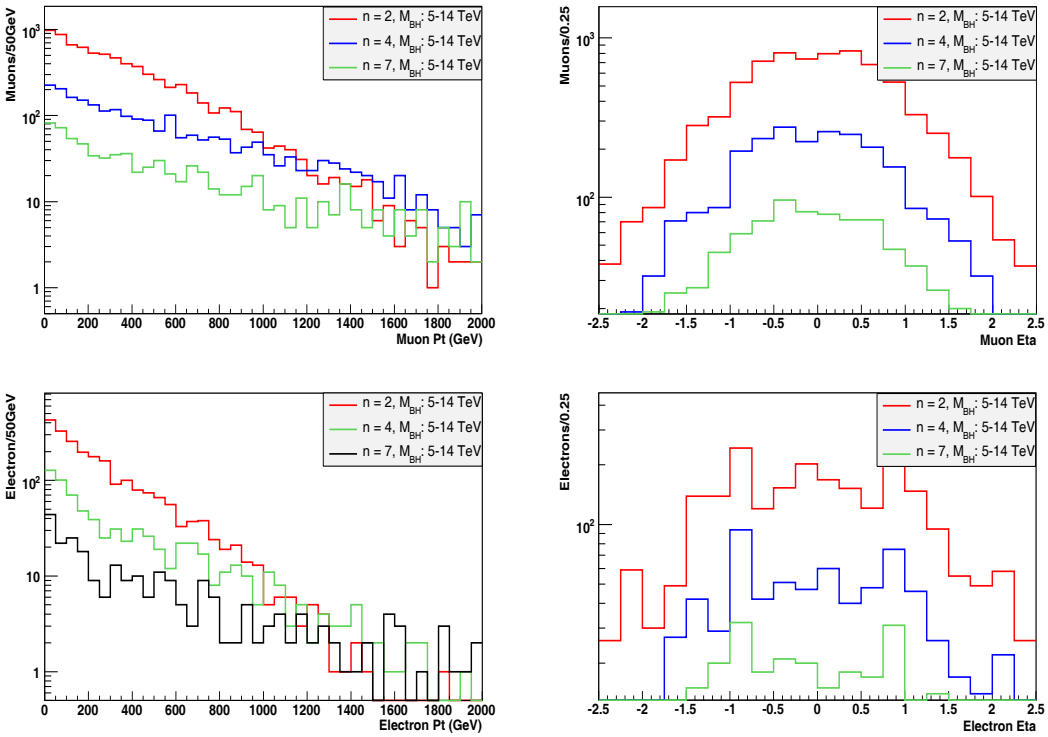

Figure A.1: p_T and η distributions of muons and electrons in black hole events

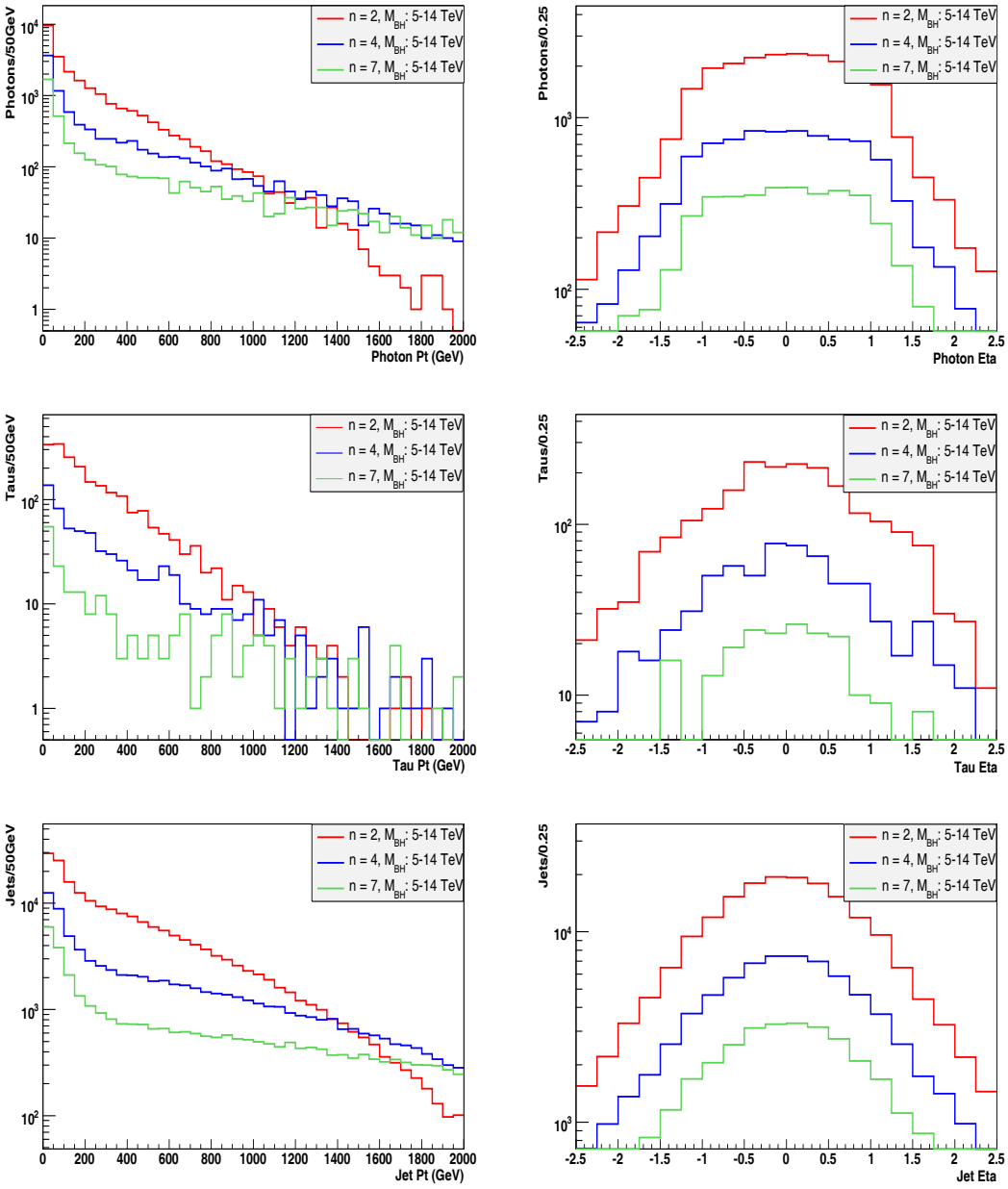

Figure A.2: p_T and η distributions of photons, taus, and jets after isolation cuts in black hole events

Appendix B

Black hole selection cuts

The histograms in this appendix show the effect of applying the selection cuts (refer to the section 4.4).

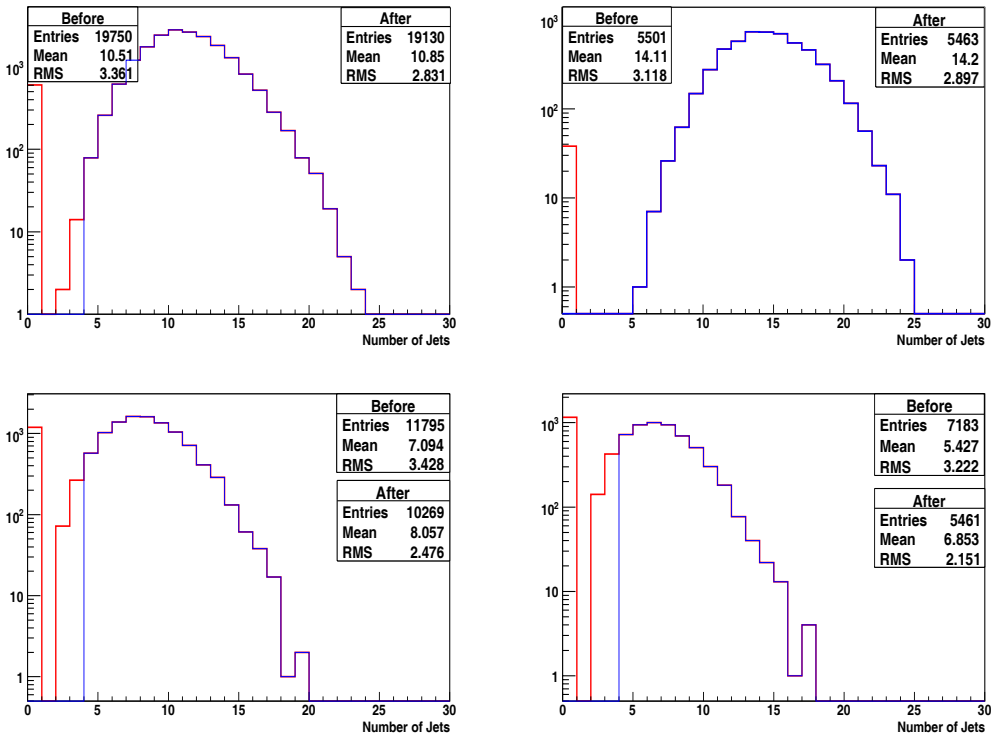

Figure B.1: Number of jets after the first selection cut.

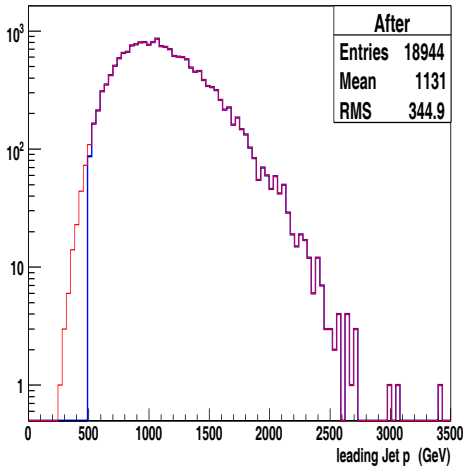

(a) Black hole 5640

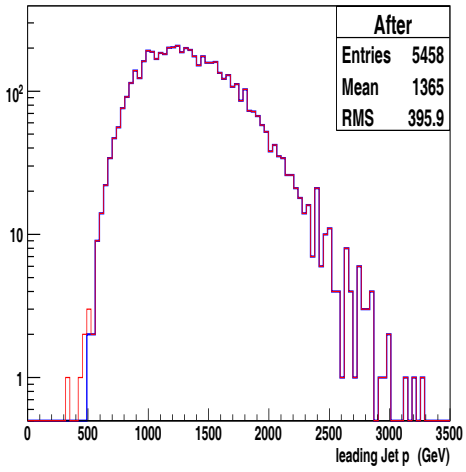

(b) Black hole 5641

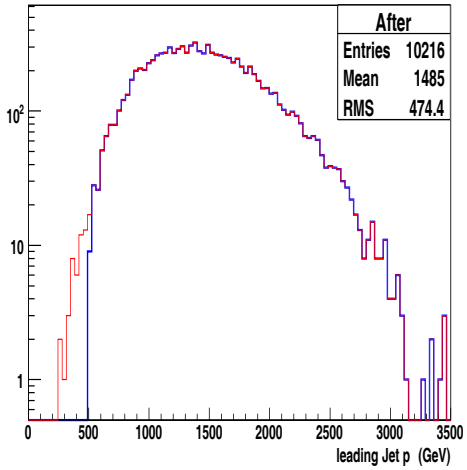

(c) Black hole 6640

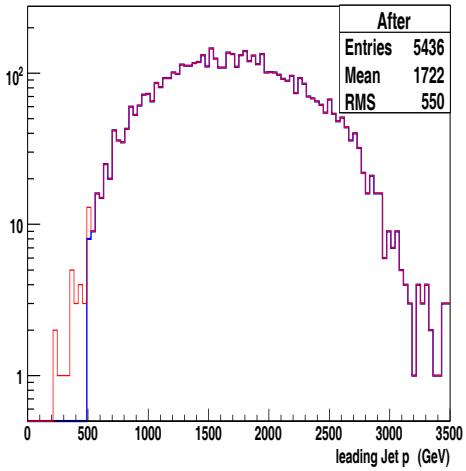

(d) Black hole 6641

Figure B.2: p_T distributions after the second selection cut to the first leading jets.

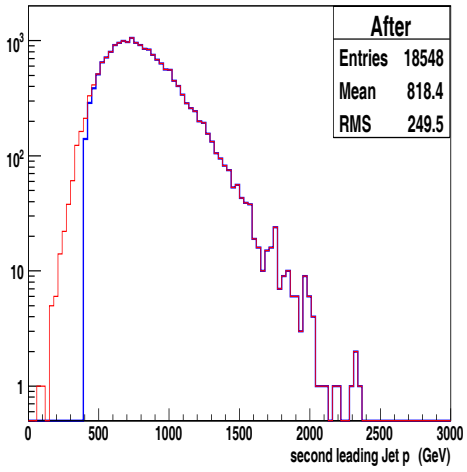

(a) Black hole 5640

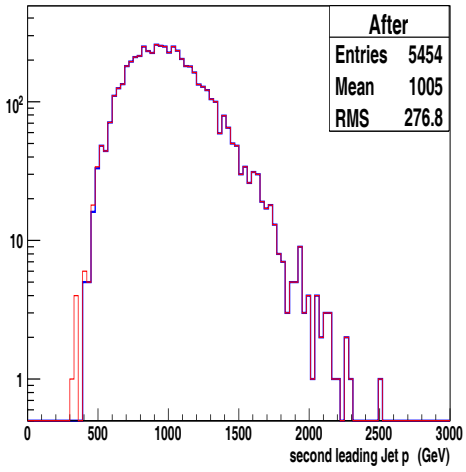

(b) Black hole 5641

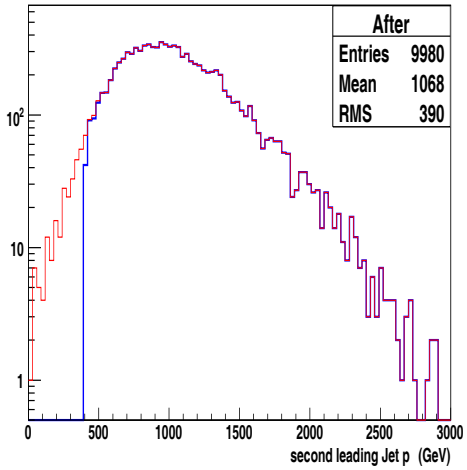

(c) Black hole 6640

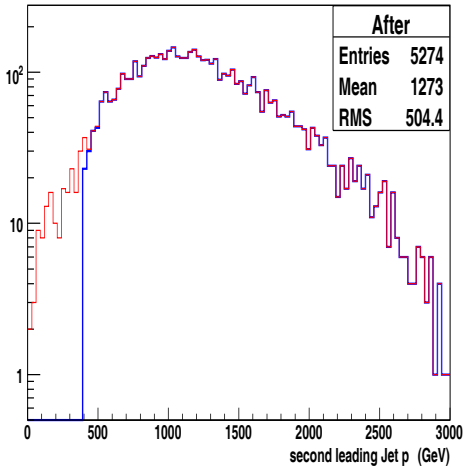

(d) Black hole 6641

Figure B.3: p_T distributions after the third selection cut to the second leading jets.

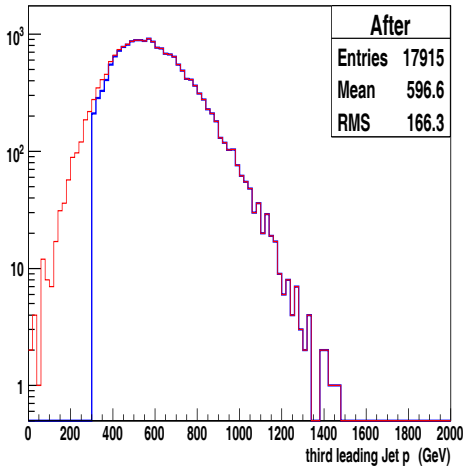

(a) Black hole 5640

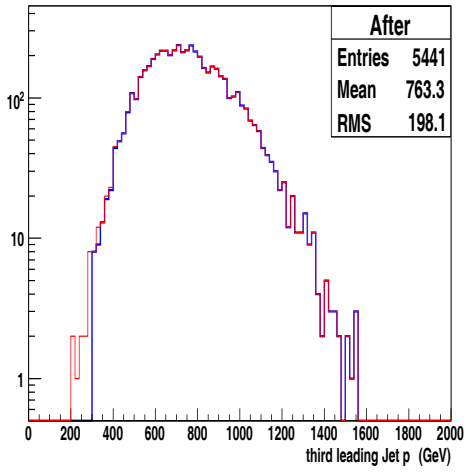

(b) Black hole 5641

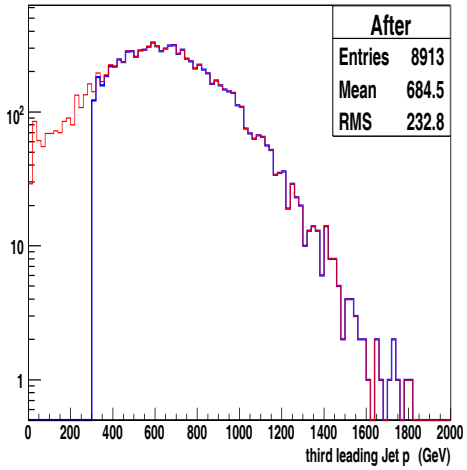

(c) Black hole 6640

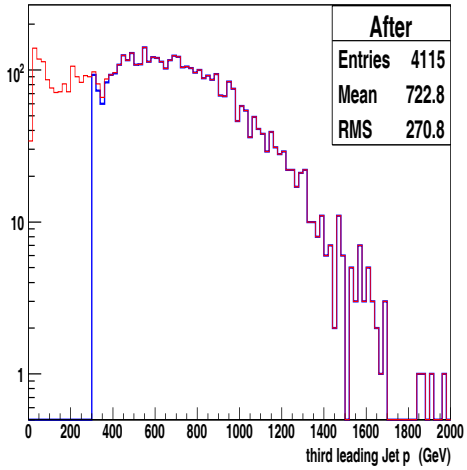

(d) Black hole 6641

Figure B.4: p_T distributions after the forth selection cut to the third leading jets.